

Simulation of Long-Period Ground Motions for the 1923 Kanto Earthquake ($M \approx 8$)

Minoru TAKEO* and Hiroo KANAMORI

Seismological Laboratory, California Institute of Technology,
Pasadena, CA 91125

(Received August 7, 1992)

Abstract

We performed numerical simulations of long-period ground motions in Tokyo for the 1923 Kanto, Japan, earthquake ($M_s=7.9$ to 8.1) which devastated Tokyo, Yokohama, and their environs, and caused more than 130,000 fatalities. We used reflection-transmission matrices and the discrete wavenumber integration method to compute ground motions for fault models placed in layered structures. The objective of this study is twofold: 1) to estimate the long-period response spectrum for the 1923 Kanto earthquake; and 2) to investigate the effects of various source parameters on the ground motion so that we can assess the variability of estimated ground motions, and apply the results to a broader class of earthquakes than just a single design earthquake specifically for the 1923 event.

The Kanto earthquake was recorded in Tokyo with a Ewing seismograph and an Imamura seismograph. The ground motions estimated by earlier investigators from these two seismograms differed significantly. This conflict can be reconciled if we assume that the solid friction of the Ewing seismograph was very high during shaking. Solid friction can reduce the resonance of the instrument, and long-period ground motions with large amplitudes can be recorded correctly. We conclude that the ground motion of the Kanto earthquake had a very large long-period component with a velocity response spectrum of 120 cm/sec (5% damping) at a period of 13 sec. The velocity response spectrum at a period of 7.5 sec is estimated to be about 50 cm/sec.

Numerical simulations produced a wide range of ground motions and response spectra, even with a given fault geometry and seismic moment. For a rupture model initiating from the southwestern end of the fault plane – the most probable epicenter of the 1923 earthquake – the computed response spectra have a range of 10 to 100 cm/sec at a period of 7.5 sec, which brackets the observed level. All the response spectra computed for this model have a peak in a period range of 10 to 13 sec. The slip distribution and the rupture direction significantly influence simulated ground motions. Large subevents in a shallow structure enhance the ground motion significantly, especially if the rupture propagation is toward the site. One of our extreme models, which has large slip of about 8 m in the shallow crust at the western end of the fault plane, can produce a large ground motion comparable to that estimated from the Ewing seismogram. Reducing the rise time or increasing the rupture propagation increases the

*On leave from the Earthquake Research Institute, University of Tokyo.

spectral amplitude at periods shorter than 5 sec. Also, if the site is located on a very soft sediment, significant (a factor of 1.4) amplification occurs. The basin structure beneath Tokyo would increase the duration of ground motion significantly. Although increased duration does not significantly affect the response spectrum, it will play an important role in the nonlinear response of structures.

Introduction

In view of the recent increase of large structures such as high-rise buildings, oil tanks, suspension bridges and offshore drilling platforms, estimation of long-period strong ground motions from several seconds to twenty seconds is becoming increasingly important.

Although it is relatively straightforward to compute long-period ground motions numerically for a given earthquake model, it is not possible to verify such simulations

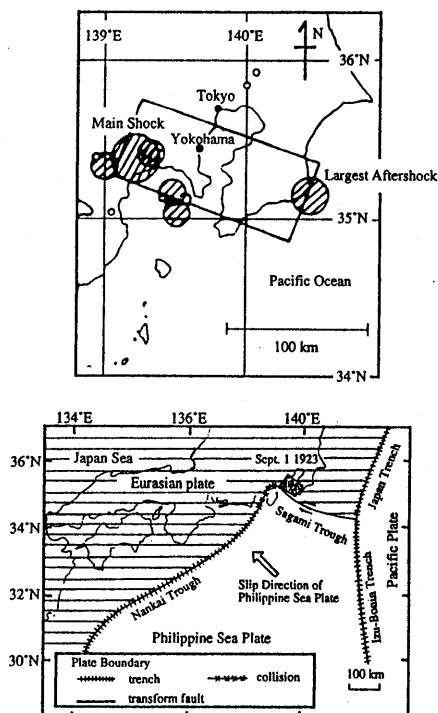


Fig. 1. The horizontal projection of the fault plane and the major aftershocks immediately after the main shock (from Kanamori, 1971a), and tectonic structure in southwest Japan (bottom figure). The fault parameters of the Kanto earthquake obtained by Kanamori (1971a, 1974) are: dip direction= $N20^{\circ}E$; dip angle= 34° ; dimension= 130×70 km; right-lateral slip=2 m; reverse dip-slip=0.65 m; rise time of dislocation=5 sec; rupture velocity=3 km/sec.

because no record of long-period ground motion in the epicentral area of a large earthquake is presently available. During the 1923 Kanto, Japan, earthquake ($M_s=7.9$ to 8.2, Figure 1) which devastated Tokyo, Yokohama, and their environs, and caused more than 130,000 fatalities, three low-gain seismographs were in operation in Tokyo. Two of them (an Omori strong-motion seismograph and an Imamura strong-motion seismograph) recorded the ground motions during the first 10 to 15 sec, but thereafter went off-scale. Another seismograph (a Ewing seismograph) recorded the ground motion almost on-scale on a turn table for about 2 min. The original seismograms of the Ewing and Imamura seismographs are shown in Figure 2. Although these records do not contain complete information of the ground motion, they can still be used for verification purposes.

Another unique aspect of the Kanto earthquake is that it occurred beneath the Kanto plain, which is covered by thick soft sedimentary layers. The combination of a large earthquake and soft sediments is fairly common, e.g. Mexico, San Francisco, and Tangshan. Also, many major cities in the world are located in a sedimentary basin with high potential for a large earthquake (e.g. Los Angeles). Since sediments play a major role in excitation and propagation of long-period ground motion in the epicentral area of a large earthquake, it is important to understand their effects on ground motions.

Considering these aspects of the Kanto earthquake, we performed numerical simulations of long-period ground motions for this earthquake. The objective of this study is twofold: 1) to estimate the response spectrum for the 1923 Kanto earthquake; and 2) to investigate the effects of various source parameters on the ground motion. Although our simulations are for models of the 1923 Kanto earthquake, there is no reason to believe that the next large earthquake near Tokyo will be a close duplicate of the 1923 Kanto earthquake. Many earthquake sequences along subduction zones demonstrate that earthquakes are very noncharacteristic from sequence to sequence. It is thus important to do a parameter sensitivity analysis so that we can assess the variability of estimated ground motions, and apply the results to a broader class of earthquakes than just a single design earthquake specifically for the 1923 event.

Observed Ground Motion

As mentioned above, a long-period Omori seismograph at Hongo, Tokyo, recorded the ground motion during the first 9.5 sec, but went off-scale when the peak-to-peak ground motion displacement reached 17 cm (Nasu, 1971a). A Ewing seismograph in Hongo, Tokyo, recorded the ground motion almost on-scale on a turn table for about 2 min (Figure 2a). Nasu (1971b) described this record, which he traced from the original disk. Morioka (1976, 1980) and Morioka and Yamada (1986) digitized the trace obtained by Nasu and estimated the SW-NE component of ground motion from this record. As shown in Figure 3, this ground motion (ED) is dominated by long-period oscillations with a period of about 13 sec which lasted for about 2 min. On the other hand, Yokota *et al.* (1989) estimated the E-W component of the ground motion using the record of an Imamura seismograph also located at Hongo (IMD in Figure 3). However, the Imamura seismogram (Figure 2b) was clipped during the first 5 minutes when the long-period

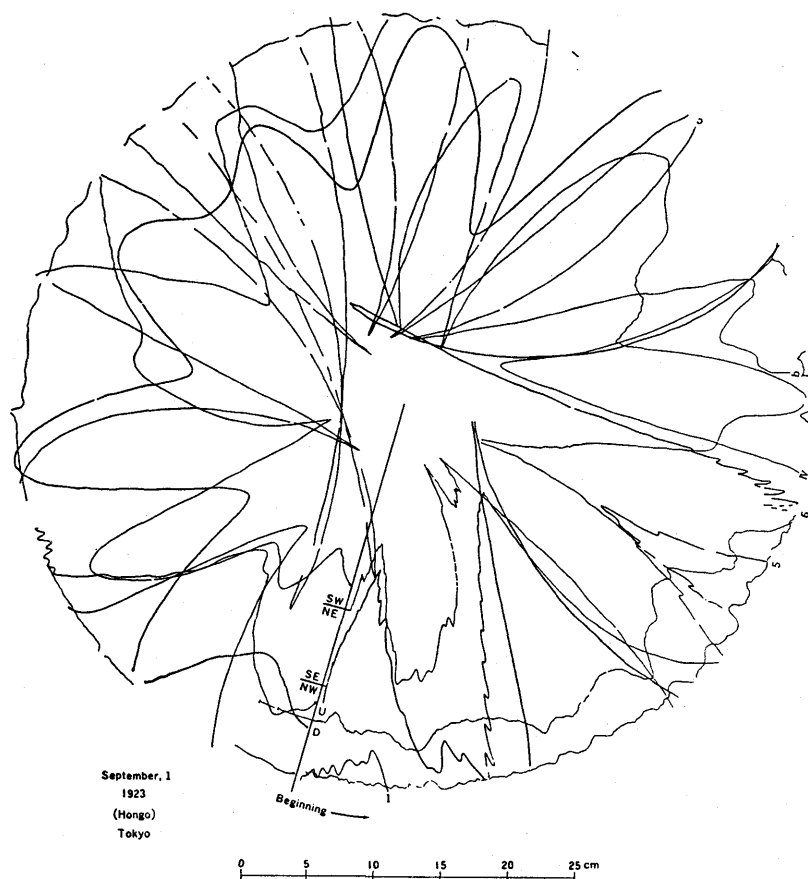


Fig. 2(a)

Fig. 2. Seismograms of the 1923 Kanto earthquake recorded in Hongo, Tokyo. (a). Seismogram recorded by a Ewing strong-motion seismograph ($T_0=6.0$ sec, $h=0.045$, $V=1.0$) on a turn table. (b). Seismogram recorded by an Imamura strong-motion seismograph ($T_0=10.0$ sec, $h=0.17$, $V=2.0$).

ground motion was recorded on the Ewing seismograph. Yokota *et al.* (1989) devised a method to restore the clipped portion of the record. The ground motion obtained by Yokota *et al.* (1989), shown in Figure 3, does not exhibit the long-period ground motion estimated from the Ewing seismogram. No explanation for this large difference has been given. However, as described in the Appendix, these apparently conflicting results can be reconciled if we assume that the solid friction of the Ewing seismograph was very large during the intense shaking of the Kanto earthquake. Solid friction can reduce the resonance of the instrument, and long-period ground motions with large amplitudes can be recorded correctly.

Also, Figure 3 shows the velocity response spectra (5% damping) computed for the ground motions estimated from the Imamura and Ewing seismograms. As shown in the Appendix, we believe that the spectral amplitude at long period (about 13 sec), estimated from the Ewing seismogram, and that at short period (about 5 sec), estimated from the Imamura seismogram, are a good approximation of the response spectrum of ground

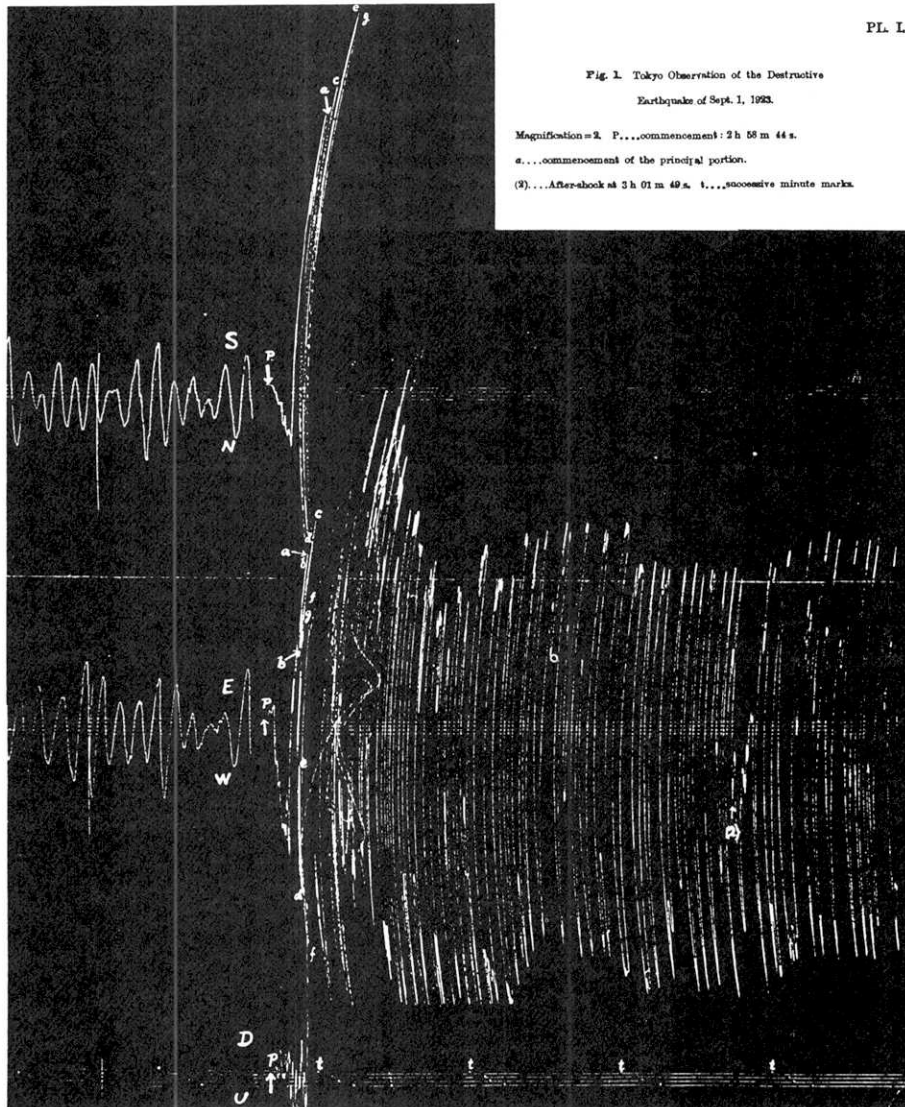


Fig. 2(b)

motion recorded at Hongo, Tokyo. The solid curve shown in Figure 3 is obtained by combining these two spectra, and will be used as a reference spectrum. Since the ground motion estimated from the Imamura seismogram is from the component with the smaller amplitude (Yokota *et al.* 1989), the response spectrum estimated from the Imamura seismogram is multiplied by 1.5 at a period range from 5 to 7.5 sec. The ground motion estimated by Morioka (1976) from the Ewing seismogram is also from the smaller component (Morioka, 1976), but considering the large uncertainties involved in the deconvolution process, we used its long-period value without modification. The solid curve shown in Figure 3 is thus somewhat subjective, but we believe that it is a reasonably good representation of the velocity response spectrum of the ground motion in Tokyo at periods longer than 5 sec.

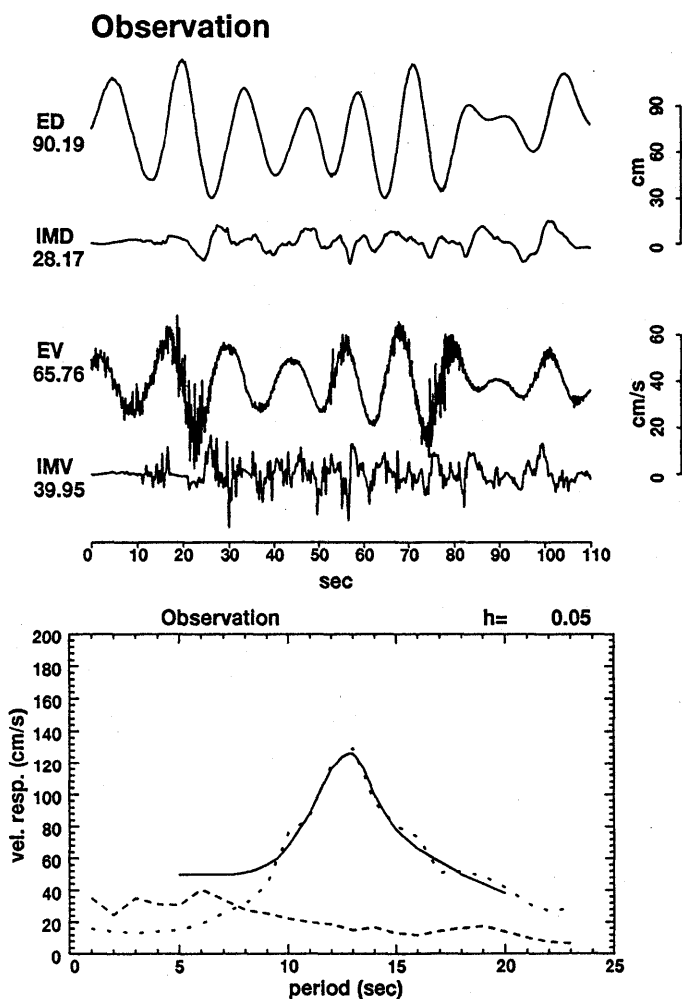


Fig. 3. Ground-motion displacements and velocities estimated from the SW-NE component of the Ewing seismogram by Morioka (1976, 1980) and Morioka and Yamada (1986) (ED, EV) and from the E-W component of the Imamura seismogram by Yokota *et al.* (1989) (IMD, IMV). Both ground motions are obtained by restoring the clipped portion of the records. The velocity response spectra (5% damping) computed for the ground motions estimated from the Imamura and Ewing seismograms are shown in the lower panel. The short dotted curve shows the response spectrum from the Ewing seismogram and the long dotted curve is from the Imamura seismogram. The solid curve is a reference spectrum obtained by combining these two spectra.

Simulation

To estimate strong ground motions successfully, we must correctly model the source process and the wave propagation effects between the source and site.

To model the propagation effects, two approaches have been used. The first is the semi-empirical method (e.g. Hartzell, 1978; Kanamori, 1979; Irikura, 1983; Takemura

and Ikeura, 1987; Heaton and Hartzell, 1989; Somerville *et al.*, 1991; Cohee *et al.*, 1991; Kanamori *et al.*, 1992) in which observed seismograms of small earthquakes are utilized as empirical Green's functions. Although the results depend on the choice of the empirical Green's functions, the method has been used successfully to model large earthquakes (e.g. Kanamori, 1979; Irikura, 1983; Kanamori *et al.*, 1992).

Several semi-empirical studies for simulating strong motions for the Kanto earthquake have been made (e.g. Yokota, 1991; Niwa *et al.*, 1992). One difficulty with the semi-empirical method is that the records of small earthquakes used as the empirical Green's function do not always have a good signal-to-noise ratio (S/N) at long period. Thus, empirical methods are not suitable for simulation of very long-period ground motions.

An alternative to the semi-empirical method is to use numerical Green's functions. A variety of tools to compute numerical Green's functions for flat-layered structures and more complex structures have been developed in the last decade, and have been used to model earthquakes using strong-motion data (e.g. Wald *et al.*, 1988; Vidale and Helmberger, 1988). Although the simulation method using numerical Green's functions does not necessarily take into account all the effects of wave propagation, it is easy to vary the source and structure parameters so that we can systematically evaluate their effects on strong motions. Several numerical studies for simulating ground motions for the Kanto earthquake have been made (e.g. Okamoto *et al.*, 1988).

To compute realistic ground motions, we need to know the slip distribution and the local dislocation time-history as a function of position on the fault plane. During the last decade, waveform inversion of strong motion and teleseismic data have been used to determine the spatial and temporal variations of slip on the fault (e.g. Hartzell and Heaton, 1983; Mori and Shimazaki, 1985; Kikuchi and Fukao, 1987; Houston, 1987; Takeo, 1988, 1992; Mendoza and Hartzello, 1989; Wald *et al.*, 1991). Several attempts have been made to systematically interpret earthquake source processes (e.g. Kikuchi and Fukao, 1987; Mendoza and Hartzell, 1988; Takeo and Mikami, 1990). These results provide constraints and guidelines for simulation of strong ground motions.

The approach we take in this study is to use numerical Green's functions computed for various crustal structures, slip distributions, rupture modes, and dislocation rise-times. Considering the uncertainties and the variabilities of the source model, we will investigate the sensitivities of the simulation to the source models by performing simulations for a large number of models. The Green's functions are calculated using reflection-transmission matrices (Kennett and Kerry, 1979) and the discrete wavenumber method (Bouchon, 1981), using an anelastic layered half-space structure (e.g., Takeo, 1985).

Crustal Structure

The crustal structures we used are listed in Table 1. The *I4* structure in Table 1 is derived from a result of an explosion experiment which revealed the depth of bedrock beneath Tokyo (Research Group on Underground Structure in Tokyo, 1989) and group velocity analysis between the Izu peninsula and Tokyo (Kudo, 1980). We also referred to a velocity structure in Sagami Bay by Yamanaka (1991). Other layered structures (*I3*

Table 1. Velocity structures used in the simulation of ground motions.

V_p	V_s	ρ	h	Q_p	Q_s
hs					
6.0	3.4	2.6	0.0	500	230
l^2					
5.6	2.9	2.5	0.0	400	200
6.0	3.4	2.6	6.1	500	230
l^3					
5.6	2.9	2.5	0.0	400	200
6.0	3.4	2.6	6.1	500	230
6.8	4.0	3.0	19.0	600	270
l^4					
2.8	1.3	2.3	0.0	200	100
5.6	2.9	2.5	2.7	400	200
6.0	3.4	2.6	6.1	500	230
6.8	4.0	3.0	19.0	600	270

and l^2) are derived by removing layers one by one, and hs is a homogeneous half space.

Source Model

The 1923 Kanto earthquake occurred on the interface between the obliquely subducting Philippine sea plate and the Eurasian plate, along the Sagami trough (Figure 1). Extensive studies on the fault model of the earthquake have been made by various investigators (e.g. Kanamori, 1971a; Ando, 1971, 1974; Matsu'ura *et al.*, 1980; Ishibashi, 1985). Kanamori (1971a, 1974) examined the far-field body and surface waves and the near-field strong motion records, and obtained the following fault model: dip direction= $N20^\circ E$; dip angle= 34° ; dimension= 130×70 km; right-lateral slip=2 m; reverse dip-slip=0.65 m; rise time of dislocation=5 sec; rupture velocity=3 km/sec. On the other hand, Matsu'ura *et al.* (1980) interpreted the geodetic data and the near-field records to obtain the static and dynamic fault parameters. Matsu'ura's fault model, which is mainly based on the geodetic data, consists of two subfaults whose strike direction is almost the same as in Kanamori's model, but the dip and rake angles differ about 10° . This difference is not important for our simulation, however. The site for which simulation is performed is very close to the fault plane, so that the location of the station relative to the radiation pattern changes as the rupture front propagates on the fault plane. Hence, the simulated ground motion is not sensitive to small changes in the mechanism. The fault area of Matsu'ura's model is about half that of Kanamori's. The slips on the west and east side subfaults of Matsu'ura's model are about four times and two times larger than the average slip of Kanamori's model, respectively, so that the total seismic moments of both models are almost the same.

For the simulations in this paper, we used Kanamori's fault model as the base model. Since the uncertainties of the various source parameters for the Kanto earthquakes are large, we will perturb many of the source parameters from the base model to investigate the sensitivities of the simulation to these parameters. Hence, the choice of the base model is not critical to the results of this paper. For example, since we will change the slip distribution on the fault plane to examine the effect of slip heterogeneity on ground

motions, a fault model like Matsu'ura's is in effect included in our simulation. Figure 1 shows the fault plane, the epicenters of the mainshock, and the major aftershocks which occurred within the 24 hours after the mainshock.

Slip Distribution

The slip distribution on the fault plane of large earthquakes is generally very complex, as shown by many investigators. For example, Kikuchi and Fukao (1987) analyzed 9 large earthquakes at subduction zones. Among them is the 1968 Tokachi-Oki earthquake, which consists of several subevents with similar seismic moments. Houston and Kanamori (1986) analyzed teleseismic P waveforms recorded for the 1985 Michoacan, Mexico, earthquake and obtained a fault rupture pattern that consists of 50 subevents with seismic moments greater than 10^{19} N•m. Mendoza and Hartzell (1989) obtained a similar slip distribution for this event. Although the overall rupture pattern on a scale of 30 km or longer is probably well determined, the details are not resolved; the resolution depends on the data used. Subevents larger than 30 km are responsible for ground motions at periods longer than several seconds. A detailed distribution of subevents is required to simulate ground motions at periods shorter than several seconds. The rise time and the rupture time also play important roles in generation of strong ground motions.

In the present simulation, we use the slip distribution of the Tokachi-Oki earthquake (Figure 4) as the base model because it is a large oblique subduction earthquake similar to the 1923 Kanto earthquake (Kanamori, 1971b). We perform many simulations while varying the slip and rupture patterns in a random fashion. Considering the large variability of the slip distribution observed for many large events, this approach is reasonable.

The 1968 Tokachi-Oki earthquake

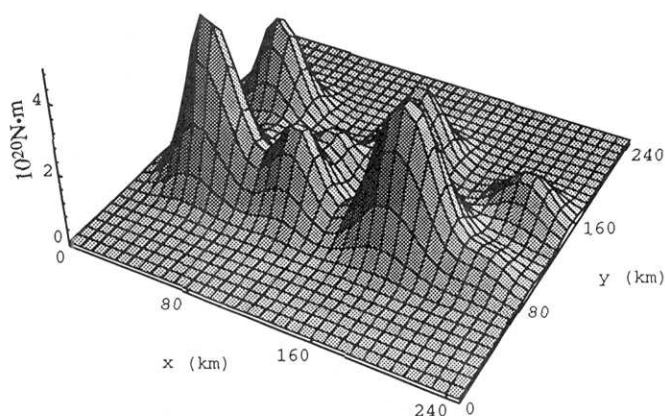


Fig. 4. Stereoscopic image of the heterogeneous distribution of dislocation sources of the 1968 Tokachi-Oki earthquake. The moment values are initially given at $20 \text{ km} \times 20 \text{ km}$ grid points. The stereoscopic image is then created by convoluting the grid pattern with an error function with a half-width of 30 km. The area shown in this figure is larger than the fault plane of the Tokachi-Oki earthquake whose length and width are 200 km and 100 km, respectively.

Our procedure to generate slip distributions to be used for simulation is as follows: We first take a $200 \text{ km} \times 100 \text{ km}$ fault plane which corresponds to the fault plane of the Tokachi-Oki earthquake, shown in Figure 4. Then, we move the pattern of slip distribution randomly on the fault plane. The part that moves out of the fault plane is wrapped around on the fault plane at the opposite side. Since the size of the fault plane of the Kanto earthquake is $130 \text{ km} \times 70 \text{ km}$, we use a $130 \text{ km} \times 70 \text{ km}$ portion of the $200 \text{ km} \times 100 \text{ km}$ plane as the model for the Kanto earthquake. We determined the slip distribution so that the average slip on the $130 \text{ km} \times 70 \text{ km}$ fault plane is 2.1 m, the average

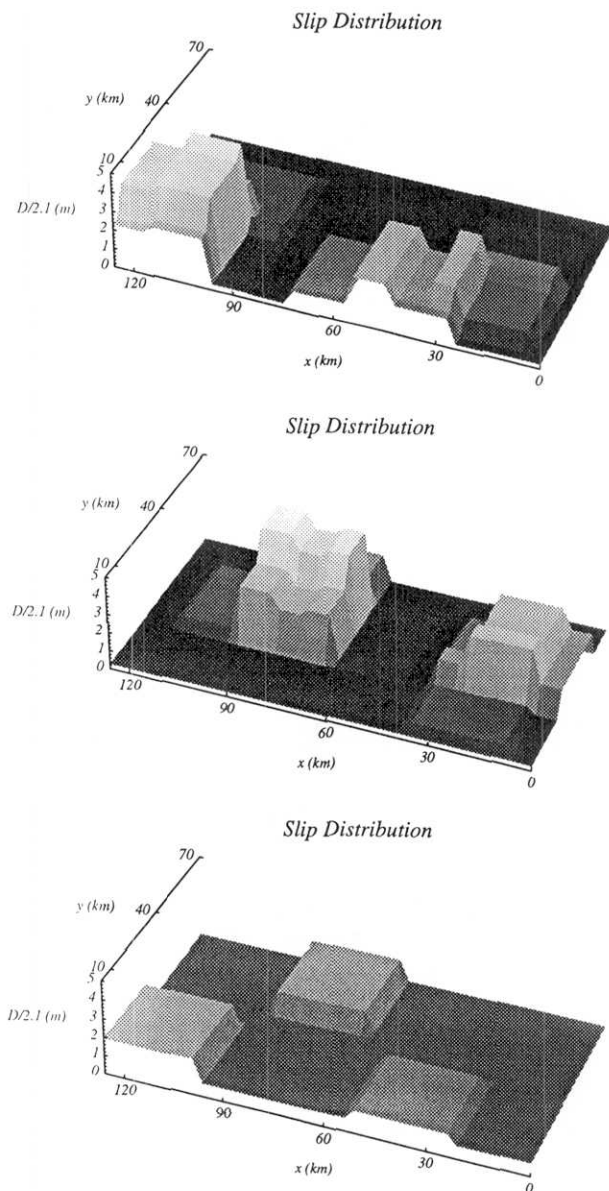
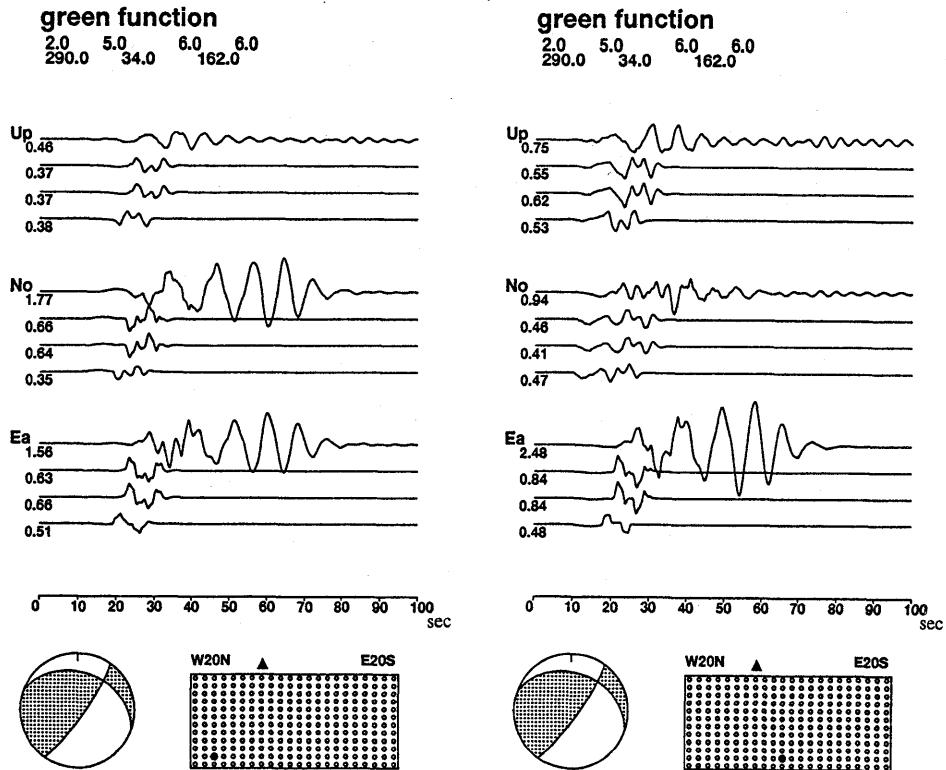


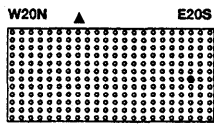
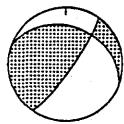
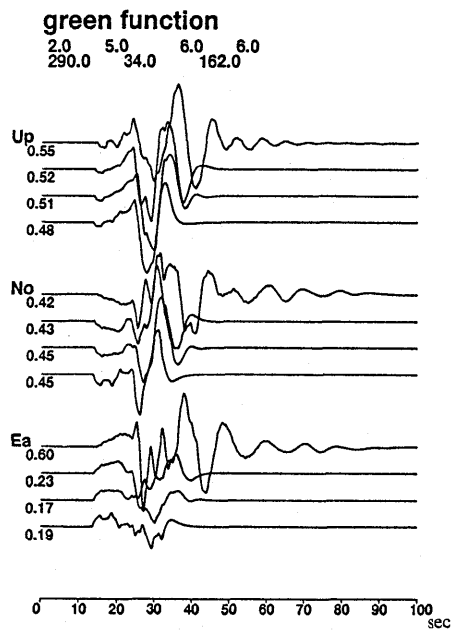
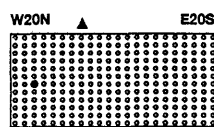
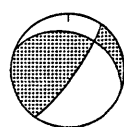
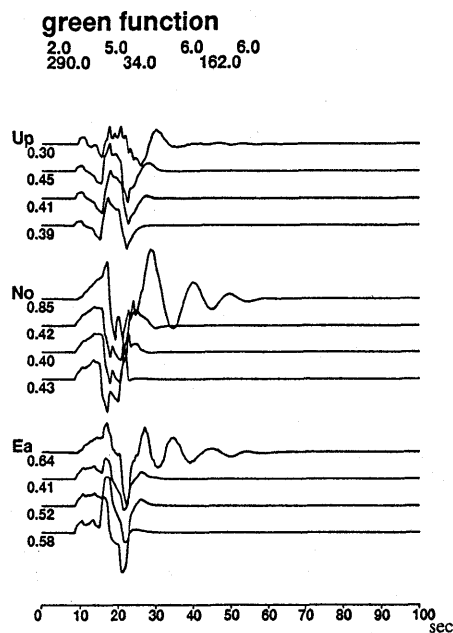
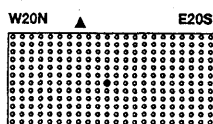
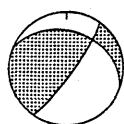
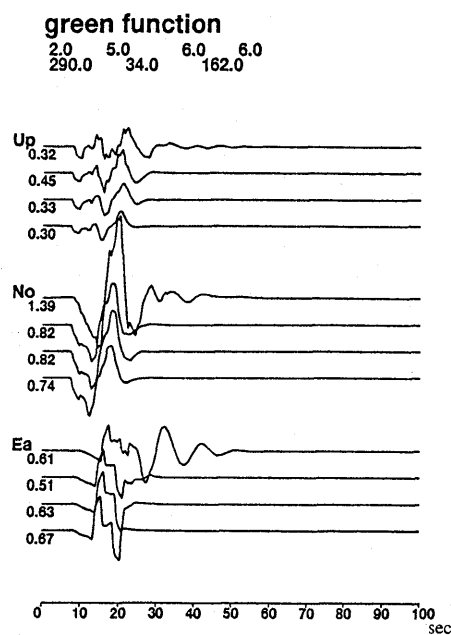
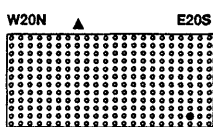
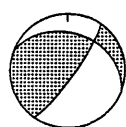
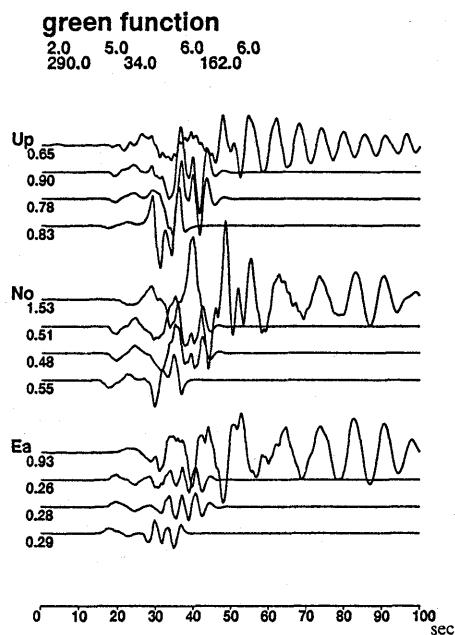
Fig. 5. Several representative examples of slip distribution used for simulations.

slip of the Kanto earthquake. Since the fault area of the Kanto earthquake is about half that of the Tokachi-Oki earthquake, the resulting slip distributions exhibit a variety of patterns, ranging from a relatively peaked distribution to a more uniform distribution consisting of similar size subevents. This procedure can produce various types of slip distributions, as illustrated by some examples shown in Figure 5.

Green's Function

Representative Green's functions used for simulations are shown in Figure 6a, which shows the velocities of ground motion at Tokyo excited by a single 6 km×6 km subfault with 2.1 m slip. The location of the source is indicated by a solid circle on the horizontal projection of the fault plane. The top trace of each group is calculated using the velocity structure *l4* in Table 1, and the second, third, and bottom traces are calculated using *l3*, *l2*, and *hs* in Table 1, respectively. The time constants of the source-time function shown in Figure 7 are $t_1=2.0$ sec and $t_2=5.0$ sec. The velocity structure in a shallow depth affects the amplitude and waveform of ground motion significantly. The low-velocity surface layer in *l4* structure causes especially large changes of the





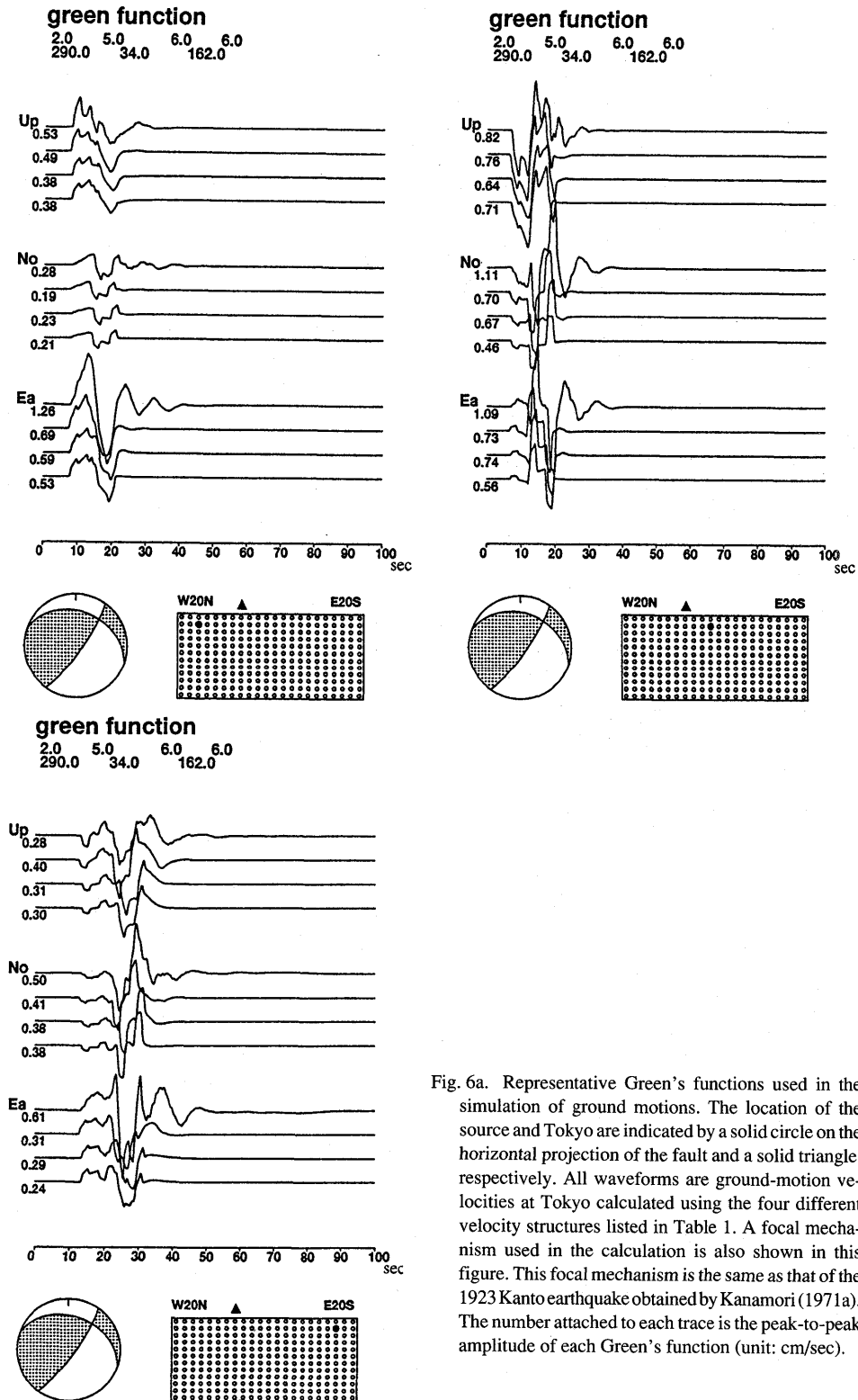


Fig. 6a. Representative Green's functions used in the simulation of ground motions. The location of the source and Tokyo are indicated by a solid circle on the horizontal projection of the fault and a solid triangle, respectively. All waveforms are ground-motion velocities at Tokyo calculated using the four different velocity structures listed in Table 1. A focal mechanism used in the calculation is also shown in this figure. This focal mechanism is the same as that of the 1923 Kanto earthquake obtained by Kanamori (1971a). The number attached to each trace is the peak-to-peak amplitude of each Green's function (unit: cm/sec).

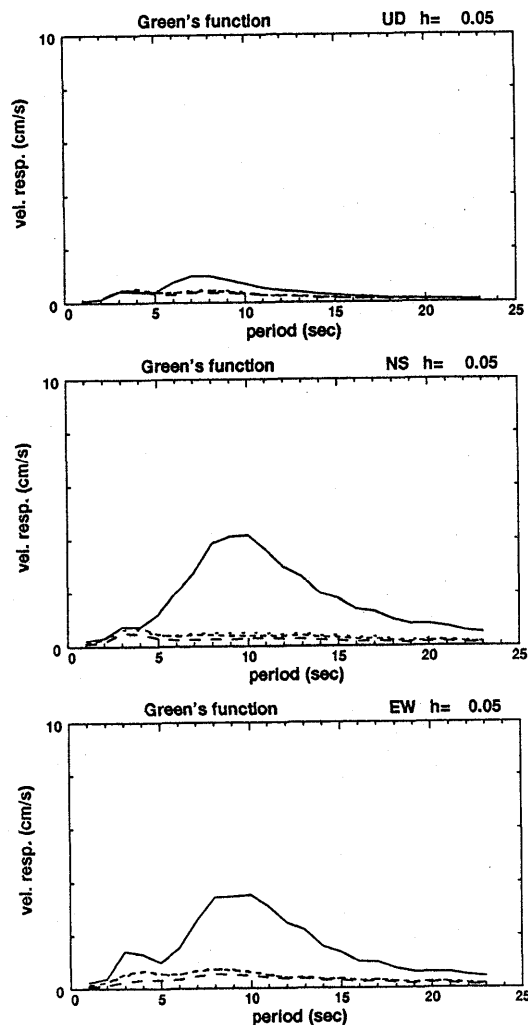


Fig. 6b. Response spectra for the representative Green's functions shown in the left uppermost of Figure 6a. The solid line is calculated using *l4* structure listed in Table 1. Other lines, which have the similar response spectra each other, are calculated using *l3*, *l2*, and *hs* structures.

waveforms. The ground motions computed for the *l4* structure that has a low-velocity surface layer are significantly larger than those for other models. Also, if the point source is placed in the shallow layer (near the bottom of the horizontal projection of the fault plane shown in Figure 6a), a large surface-wave with a period of 7 sec is excited (top three figures of Figure 6a).

Figure 6b shows the response spectra for representative Green's functions shown in Figure 6a. Note that the peak response is at 8 to 10 sec.

Superposition

To compute the ground motion for the entire fault, we divided the fault plane into 43×23 subfaults, each having an area of $3 \text{ km} \times 3 \text{ km}$; the source process in each subfault

is represented by a point dislocation source with a source-time function as shown in Figure 7. The time constants t_1 and t_2 correspond to the rupture time and the rise time for each subfault, respectively. This source-time function corresponds to the equivalent point source-time function for a unilateral rupture. For bilateral and circular rupture modes, the source-time function for each subfault should be varied spatially. In our simulation, however, we used, for simplicity, the same source-time function as shown in Figure 7 for all the subfaults. To reduce the computation time, we used 22×12 subfaults (area, 6 km \times 6 km) in several simulations. In this case, a small amplitude wave with a period approximately the same as the rupture time across each subfault often appeared in the simulated ground motion. This wave is probably spurious, caused by the too coarse division of the fault plane. Simulations which use larger subfaults than this (e.g. Okamoto *et al.*, 1988) may have some numerical noise at periods less than several seconds.

The i -th component of ground motion from all the subfault is

$$u_i(t) = \sum_{j=1}^N m_j \int g_{ij}(t - t_{sj}; \tau) f(\tau; t_1, t_2) d\tau \quad (1)$$

where N is the total number of subevents, and m_j and t_{sj} are the seismic moment and the onset time at the j -th subfault, respectively, and $g_{ij}(t; \tau)$ is the synthetic Green's function for the i -th component of ground motion excited by the rupture on the j -th subfault at $t = \tau$. The function $f(t; t_1, t_2)$ is the source-time function shown in Figure 7.

The time constant t_{sj} is given by

$$t_{sj} = r_j / v_r + t_{rmd} \quad (2)$$

where v_r is the rupture velocity, r_j is the distance from the hypocenter to the j -th subfault, and t_{rmd} is a random number ranging from $-0.1r_j/v_r$ to $0.2r_j/v_r$, which is included to add

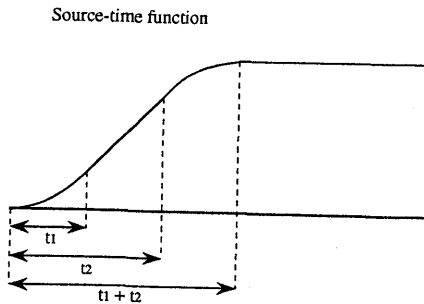


Fig. 7. The source-time function used in simulations. t_1 and t_2 are the time for the rupture front to propagate through a subfault and the rise time of dislocation, respectively. This function is quadratic in time for the first part (between 0 and t_1) and the last part (between t_2 and t_1+t_2), and linear in time for the middle part (between t_1 and t_2).

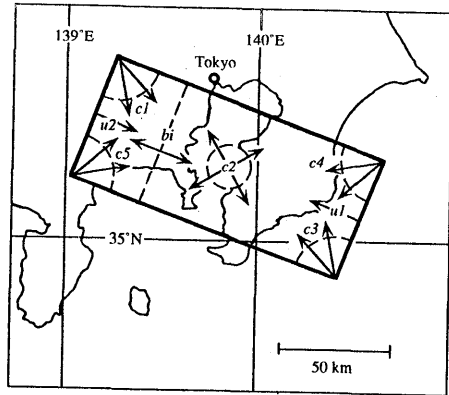


Fig. 8. Rupture propagation modes used for simulations. *bi* is a bilateral rupture. *u1* and *u2* indicate two kinds of unilateral rupture. *c1*–*c5* are five circular rupture modes which initiate from different points on the fault plane.

irregularity to rupture propagation. Since the rupture velocity of an earthquake is usually slower than the shear wave velocity in the source area, we use a non-symmetrical range for t_{rmd} . We used eight different rupture propagation modes to investigate the variation of the response spectra due to directivity. These eight modes are illustrated in Figure 8.

Sensitivity Analysis

Velocity Structure

To investigate the effect of the surface layer on the waveforms, we computed ground motion velocities for the four different velocity structures listed in Table 1. In these computations we used a uniform fault with 2.1 m slip. Figure 9 shows the ground-motion velocities for the three rupture modes: bilateral (*bi*) and two circular rupture modes *c3* and *c5*. The top trace of each group is calculated using *l4* structure, and the second, third, and bottom traces are calculated using *l3*, *l2*, and *hs*, respectively. In these simulations, the rupture velocity (v_r in equation (2)), t_1 , and t_2 are assumed to be 3 km/sec, 2 sec, and 5 sec, respectively, and the fault plane is divided into 264×6 km \times 6 km subfaults. The velocity response spectra (5% damping) of these ground motions are shown in Figure 10. The line types of the response spectra correspond to those of the waveforms in Figure 9. The waveforms and the response spectra for all the structures are similar except for the *l4* case. The spectral amplitudes are smaller than the reference spectral amplitude shown in Figure 3 for all cases. This suggests that some irregularities in slip distribution are required to excite ground motions comparable to those observed.

Slip Distribution

To further examine the effect of the low-velocity surface layer and the slip distribution, we compared the response spectra for *l4* and *hs* structures. We varied the slip distribution on the fault plane following the procedure described in the previous section. Figures 11 and 12 show the response spectra for all the rupture modes using *hs* and *l4* structures, respectively. In these simulations, we use 989×3 km \times 3 km subfaults to calculate the ground motions. The rupture velocity (v_r), t_1 , and t_2 are fixed at 3 km/sec, 1 sec, and 5 sec, respectively. Each graph shows 180 response spectra for different slip distributions. More than 600 response spectra are calculated for each rupture mode, but all of them are within the range shown in Figures 11 and 12.

In general, if the slip extends to the surface layer, the response spectra for the horizontal components increase three times, but those for the vertical component are not affected significantly. The amplification factor for a vertically incident *SH* wave at the surface layer is only about 1.5, and cannot explain the difference of the response spectra between *hs* and *l4*. In special cases such as the NS component for *c5* rupture mode or the EW component for *c3* rupture mode, however, the difference in the response spectra between the two cases reaches 6 to 8 times. Only in the case of the *c3* rupture mode does the vertical response spectrum for the *l4* structure become twice as large as that for the *hs* structure. Except in extreme cases, the variation of response spectrum due to changes in slip distribution is about a factor of 4.

The response spectra for half space *hs* are consistently smaller than the reference

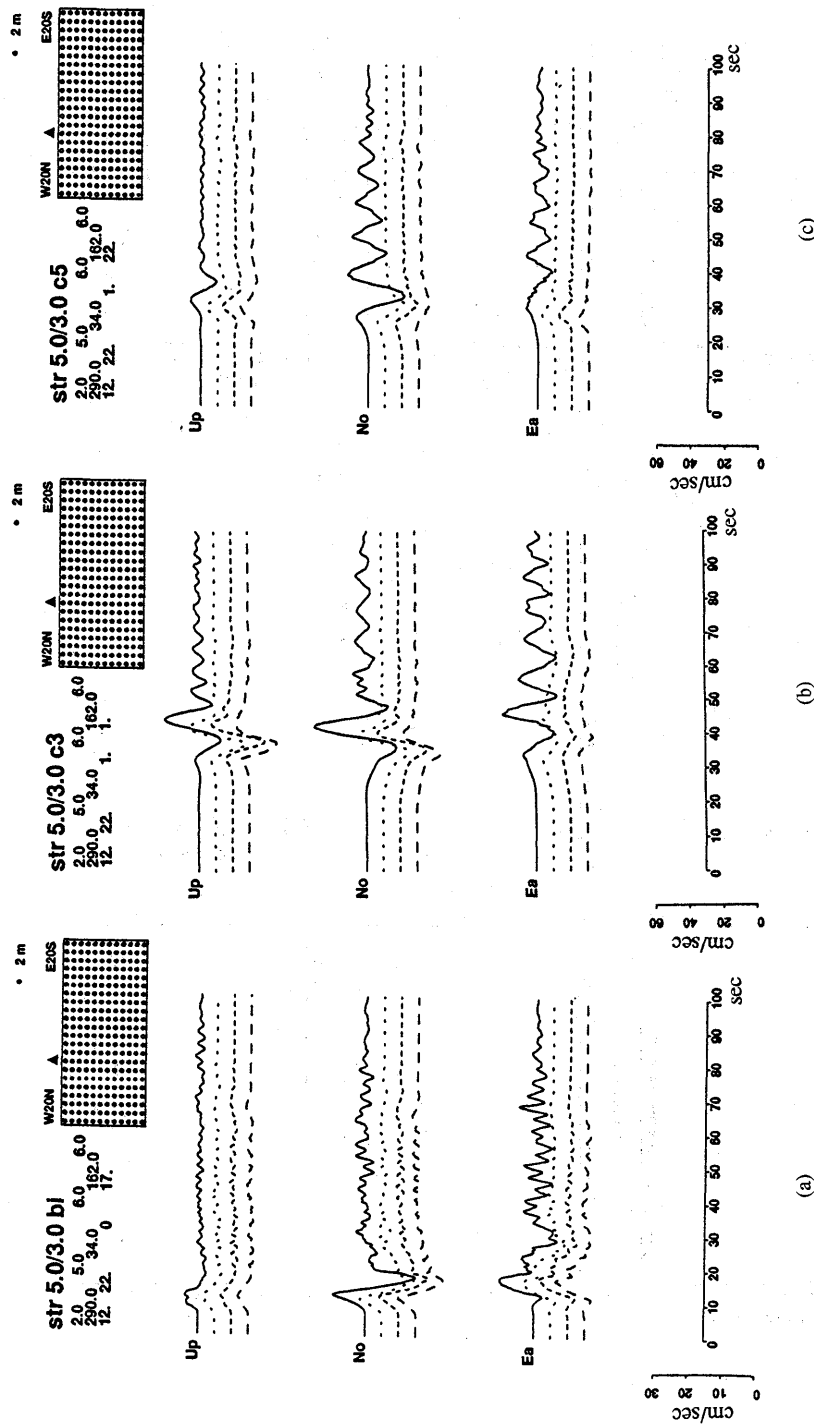


Fig. 9. Ground-motion velocities at Tokyo excited by a homogeneous slip on the fault plane computed for a bilateral rupture mode (a), and two circular rupture modes (b and c). Starting points of the rupture are shown by solid circles on the fault plane. The last two characters in the first line of comments indicate the rupture mode illustrated in Figure 8.

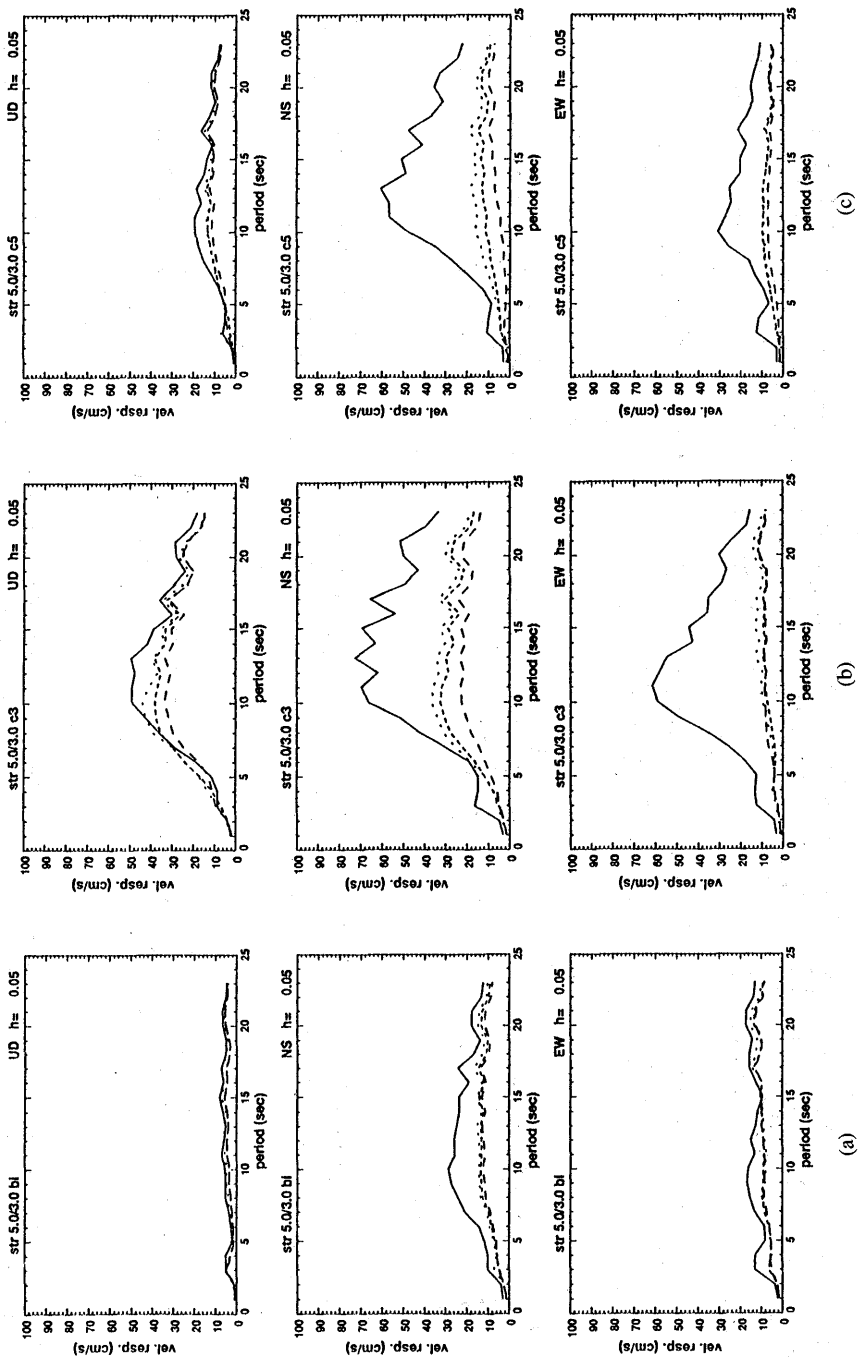


Fig. 10. Velocity response spectra (5% damping) of ground motions in Figure 9. Line type of the response spectrum corresponds to that of the waveform in Figure 9.

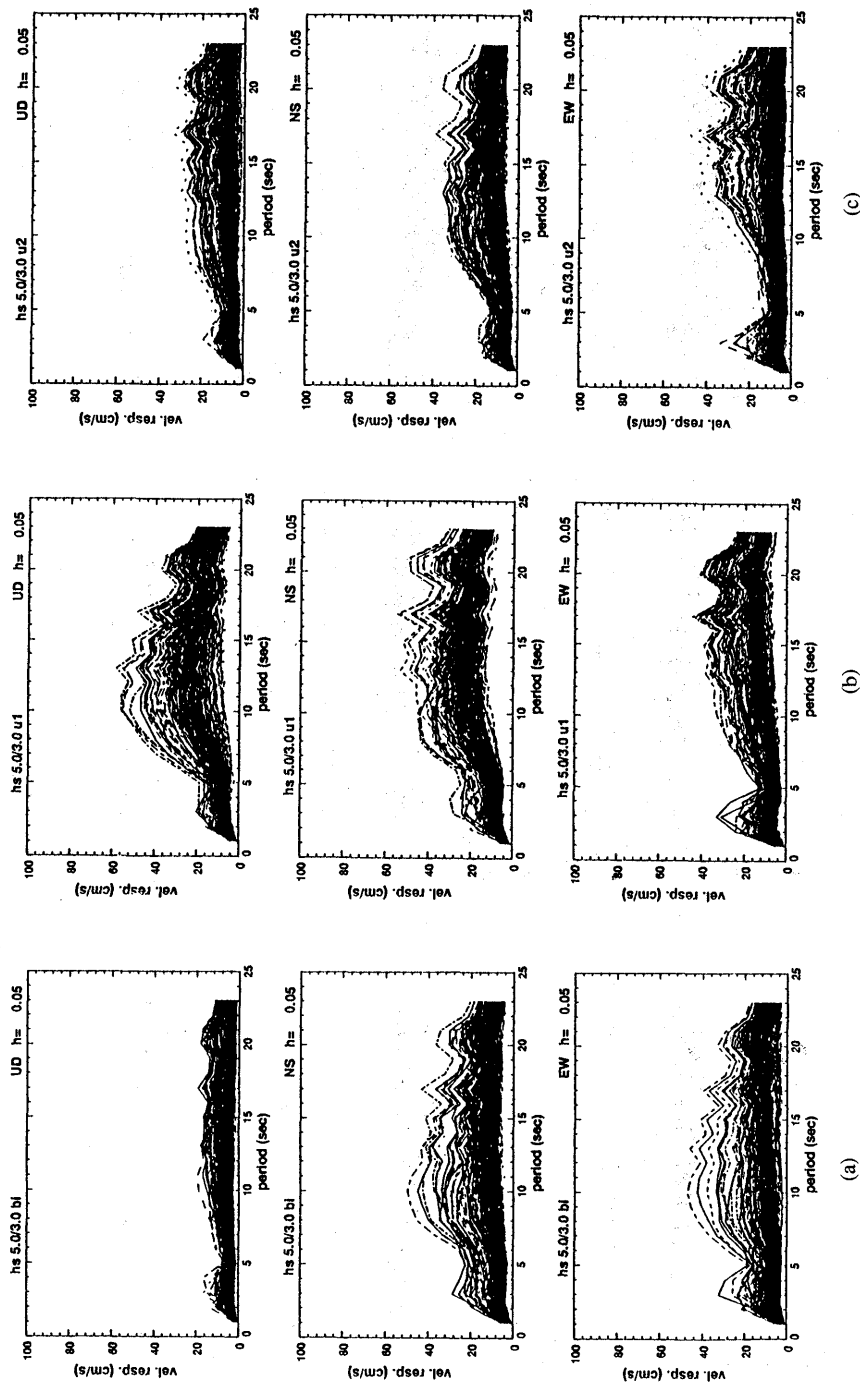
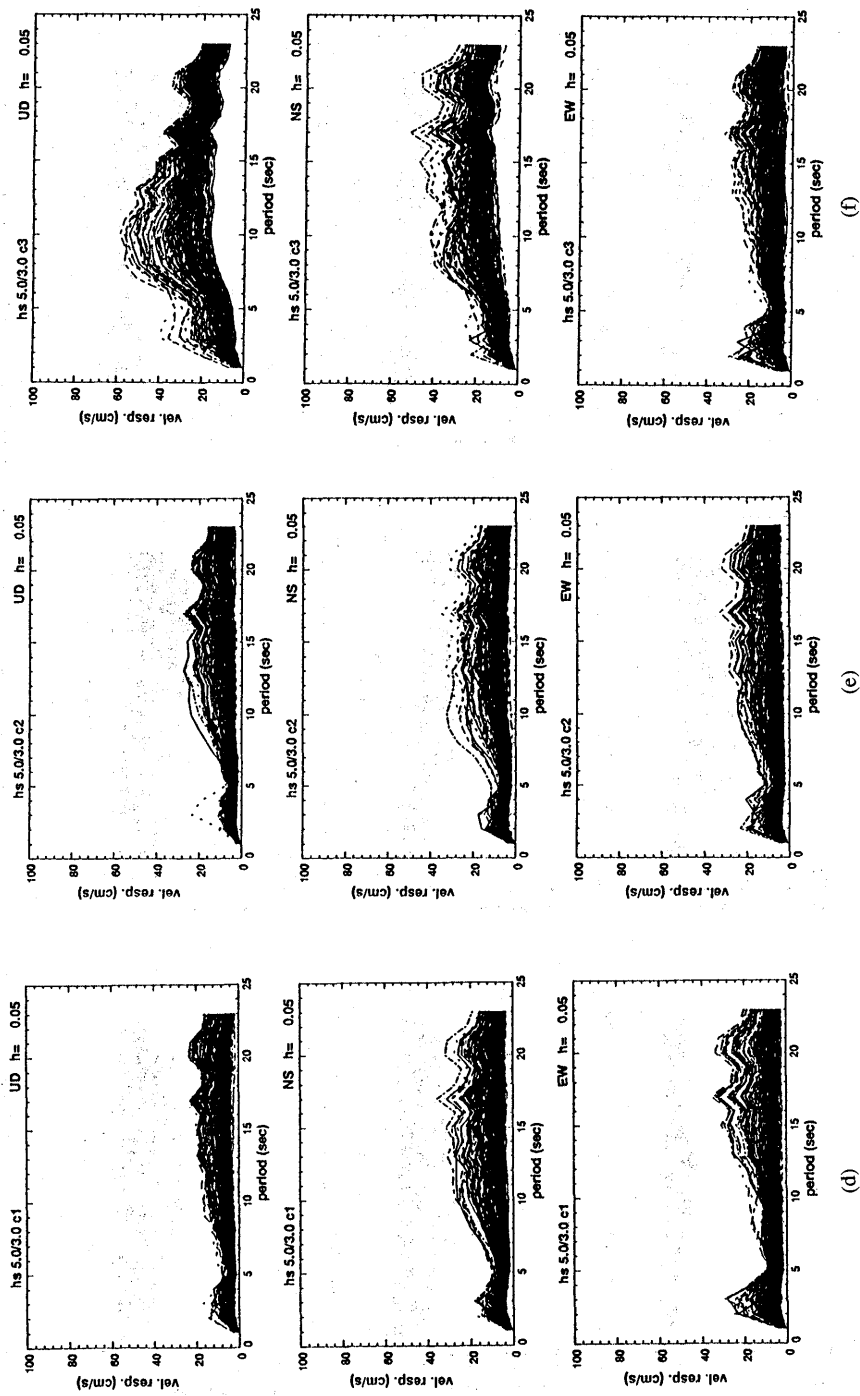


Fig. 11. Velocity response spectra (5% damping) of ground motions. The homogeneous half space structure h_s in Table 1 is used in the calculation. The response spectra for eight rupture propagation modes illustrated in Figure 8 (bl , $u1-u2$, $cl-c5$) are shown in Figures 11a to 11h. Each graph includes 180 response spectra of ground motions calculated for different slip distributions on the fault plane.



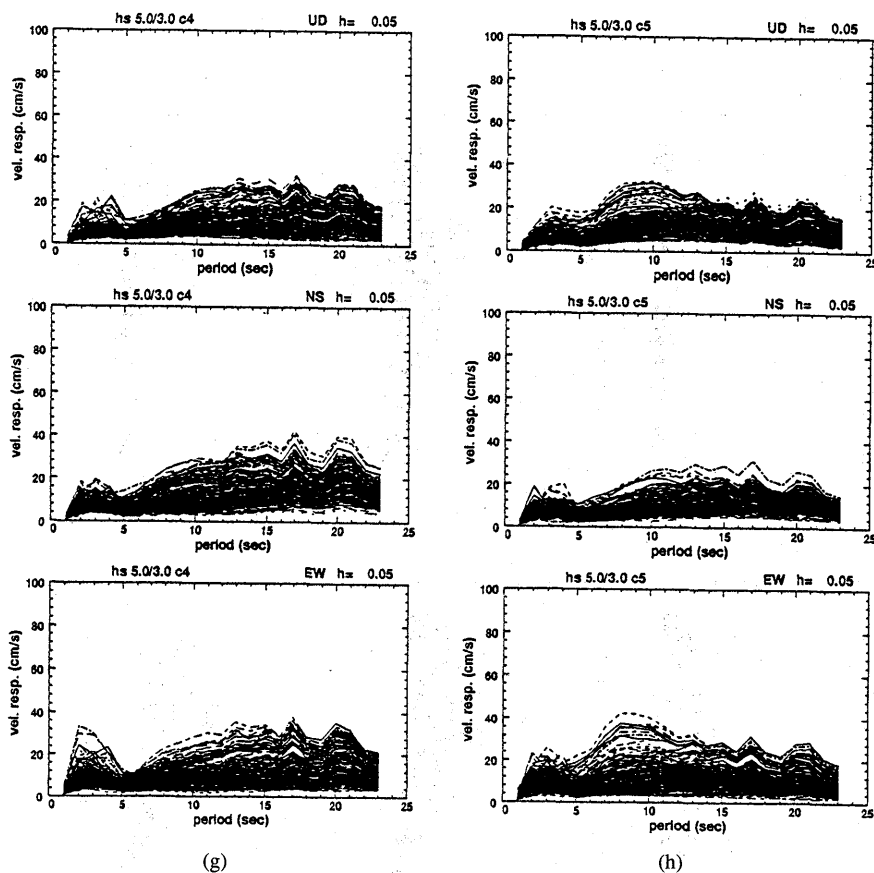


Table 2. Amplification factors for velocity response spectrum (5% damping).

subject	factor on velocity response spectrum
low velocity surface layer	~ 1 (vertical component) (maximum ~ 2) ~ 3 (horizontal component) (maximum ~ 8)
rupture velocity (2.5 km/s - 3.5 km/s)	~ 1.2 (increase every 0.5 km/s)
rise time (3.0 s - 7.0 s)	~ 2 (for shorter than 7 s) ~ 1.5 (for longer than 7 s) (decrease every 2 s)
distribution of slip	~ 4
rupture propagation	~ 2

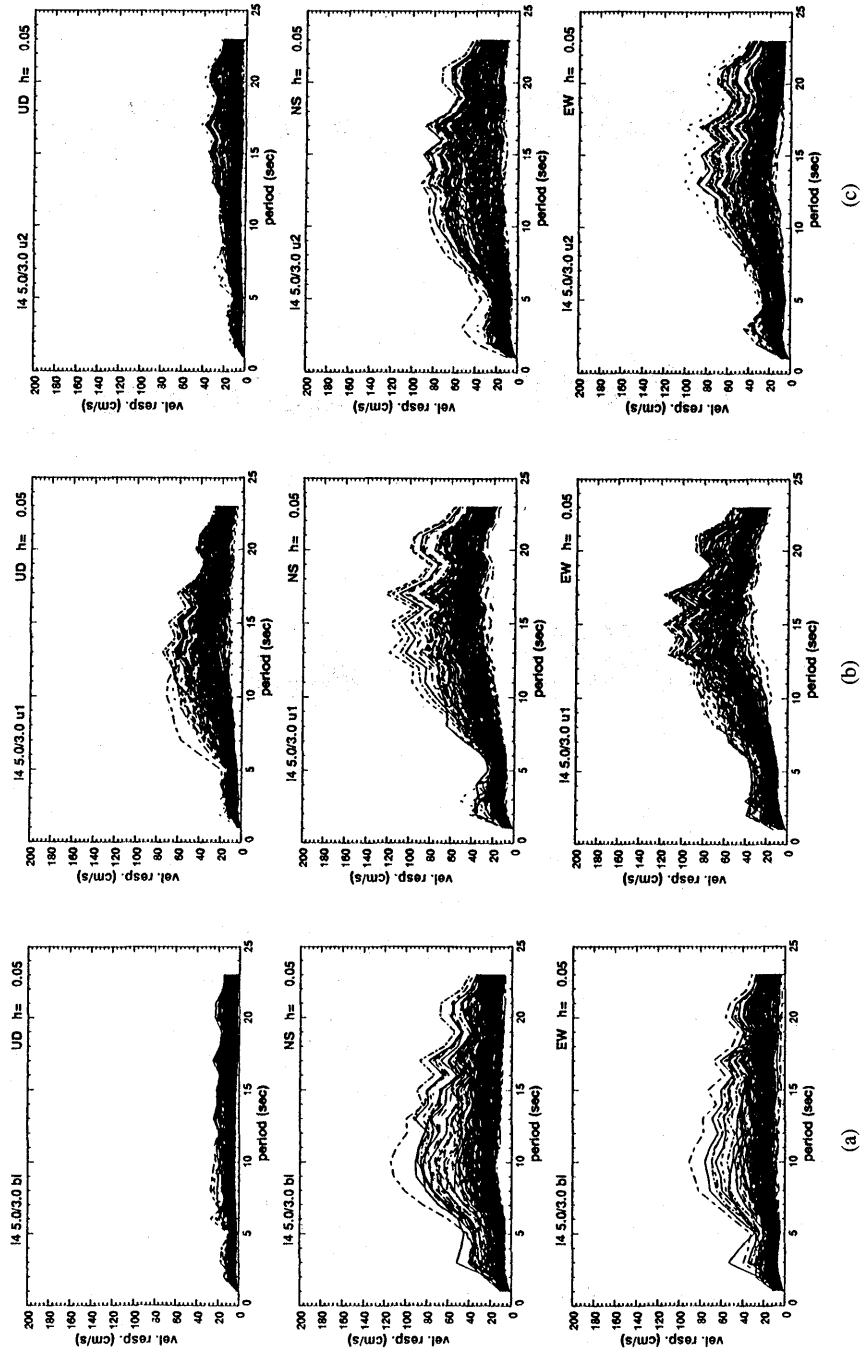
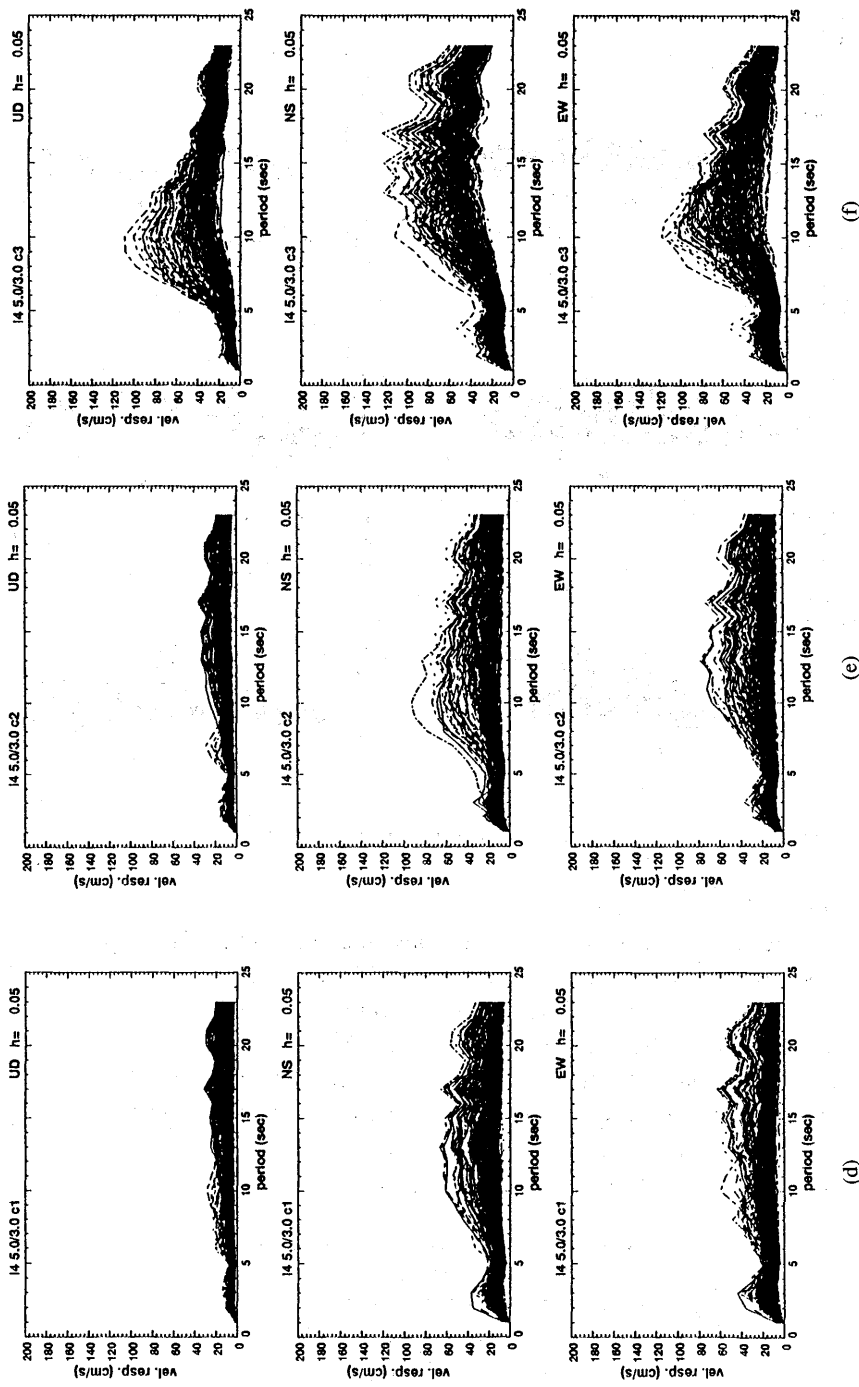
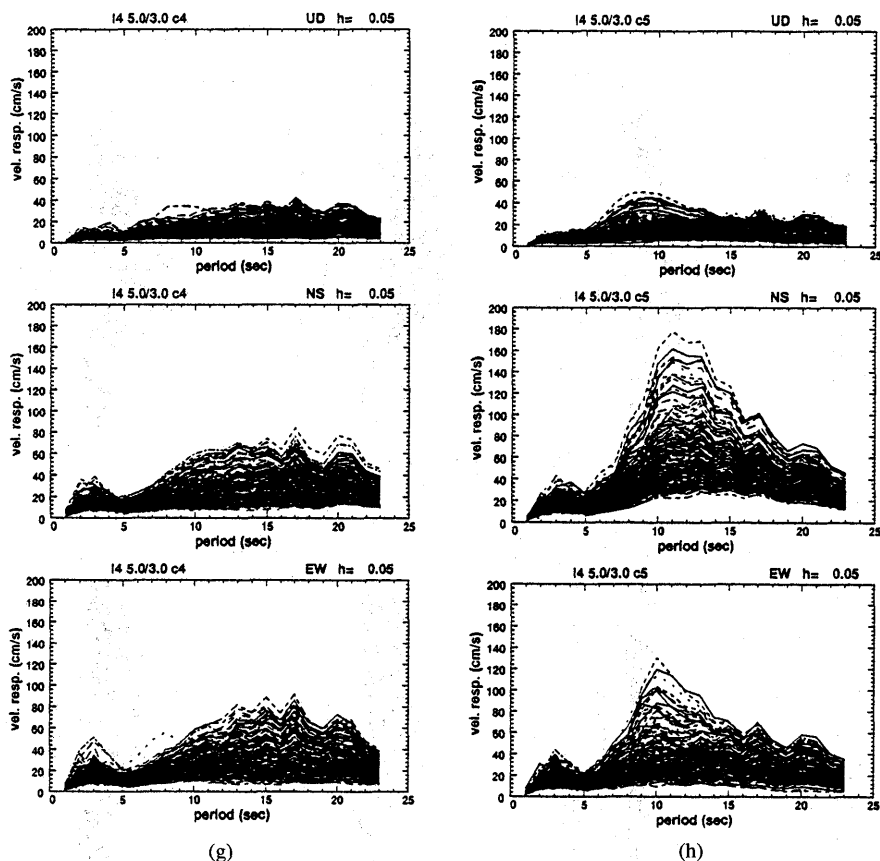


Fig. 12. Velocity response spectra (5% damping) of ground motions. 14 structure in Table 1 is used in the calculation. The range for the vertical axis of Figure 12 is twice as large as that of Figure 11.





spectrum. The reference spectrum is in the middle of the range of the spectra for $l4$.

Rupture Velocity and Rise Time

Figure 13 compares the velocity response spectra computed for rupture velocities v_r of 2.5 km/sec, 3.0 km/sec and 3.5 km/sec. The bilateral rupture mode (*bi*) is used for this computation. We examined the effects of rupture velocity change for all the rupture propagation modes illustrated in Figure 8. The effects, however, are not as large as those of the slip distribution or the low-velocity surface layer. We roughly estimate that the increase in the response spectra is 1.2 when v_r changes from 2.5 km/sec to 3.0 km/sec or from 3.0 km/sec to 3.5 km/sec.

The change in the rise time (t_2 in equation (2)) causes a larger variation in the

Table 3. Velocity structures used for estimation of the effects of a sedimentary layer.

V_p	V_s	ρ	h	Q_p	Q_s
<i>IS</i>					
1.83	0.7	2.0	0.0	100	50
2.8	1.3	2.3	1.0	200	100
5.6	2.9	2.5	2.7	400	200
6.0	3.4	2.6	6.1	500	230
6.8	4.0	3.0	19.0	600	270

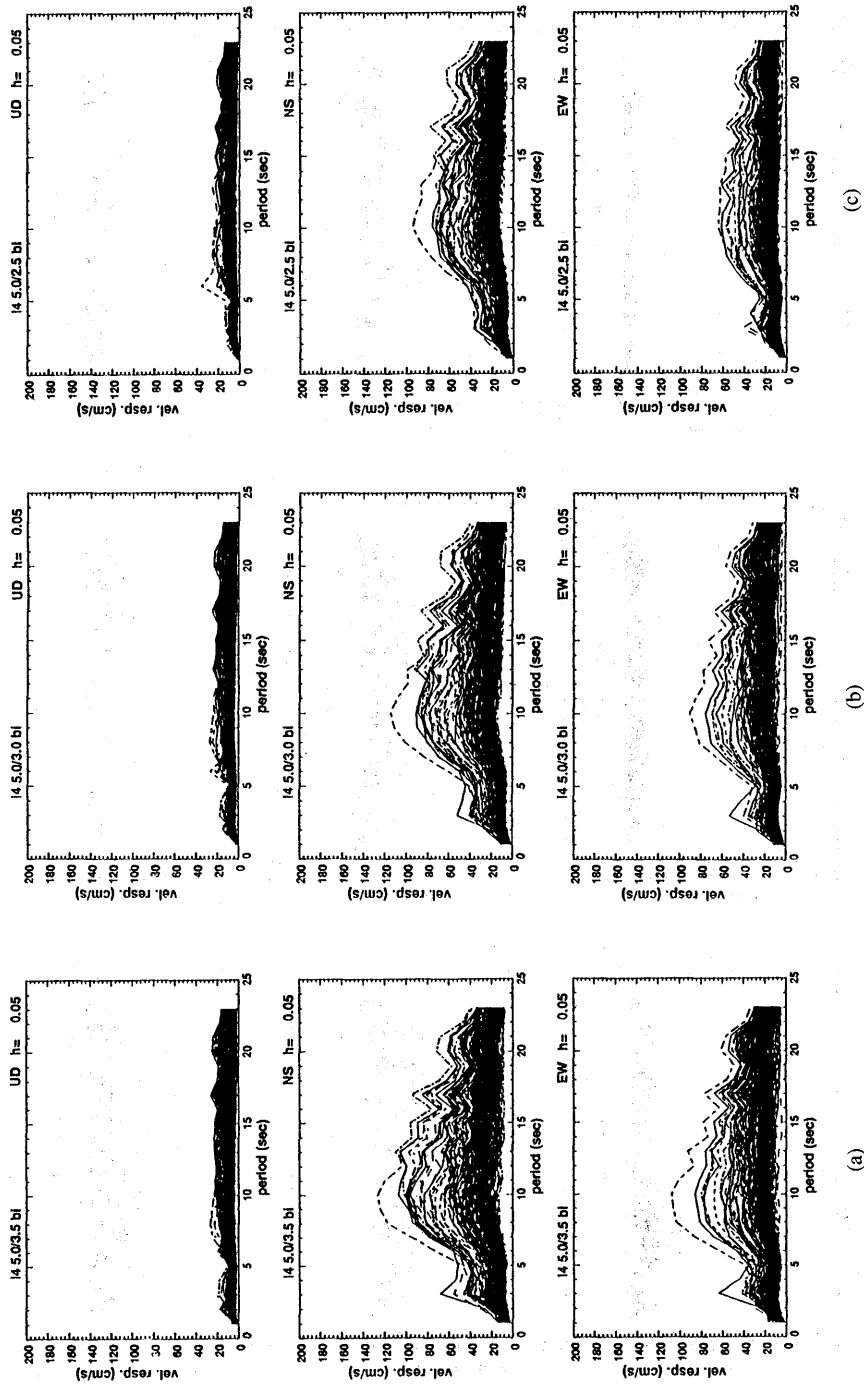


Fig. 13. Velocity response spectra (5% damping) of ground motions for the bilateral rupture case with a rupture velocity of 3.5 km/sec (a), 3.0 km/sec (b), and 2.5 km/sec (c).

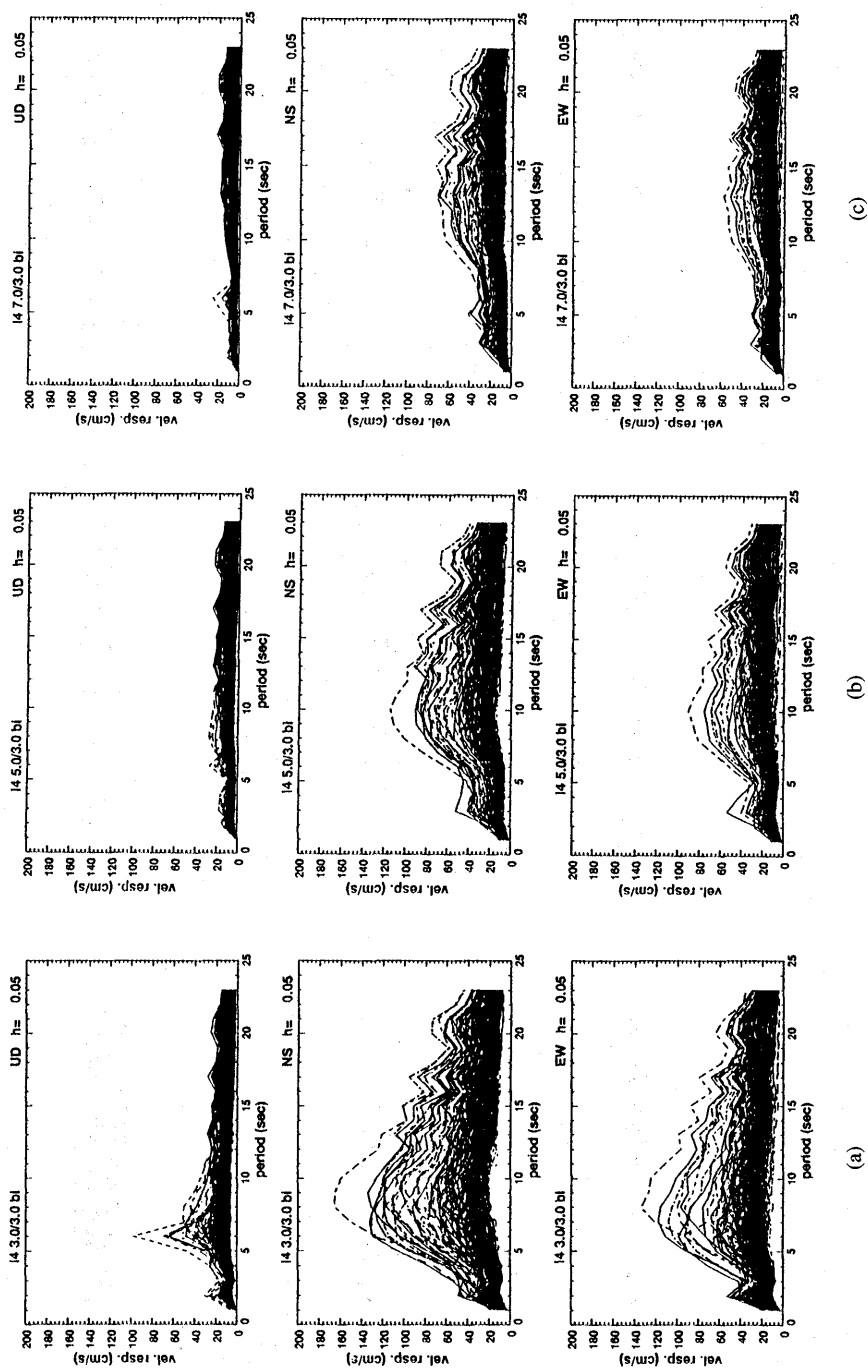


Fig. 14. Velocity response spectra (5% damping) of ground motions for the bilateral rupture case with a rise time of 3 sec (a), 5 sec (b), and 7 sec (c).

response spectra than the change in v_r . The response spectra for the bilateral rupture mode for a change in t_2 from 3 sec to 7 sec are shown in Figure 14. The spectra at periods shorter than 7 sec increase by a factor of two when t_2 changes from 5 sec to 3 sec or from 7 sec to 5 sec. However, the amplification at periods longer than 7 sec is about 1.5.

The response spectra vary by a factor of 2 for different rupture modes, except for a few special cases such as the NS component of the $c5$ rupture mode (see Figure 12). The spectral hole around 5 sec (see Figures 12 and 13) is caused by the fixed rise time of 5 sec in the source-time function, and is artificial to some extent. This hole moves as the rise time is varied, as seen in Figure 14. In general, a narrow peak of the response spectrum suggests a long harmonic oscillation at the period and a broad peak corresponds to an impulsive waveform.

The effects of various rupture parameters on the velocity response spectra discussed in this section are summarized in Table 2.

Soft Surface Layer

A thick sedimentary layer covers the area around Tokyo bay (e.g., Shime *et al.*, 1976). To investigate amplification effects due to the sedimentary layer ($v_s=0.7$ km/sec),

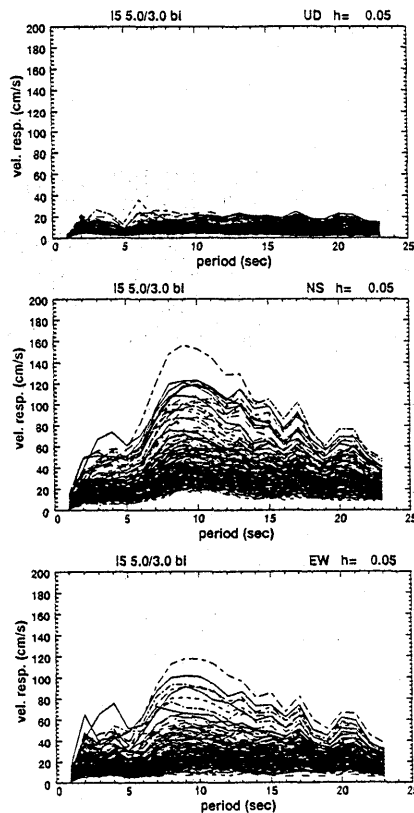
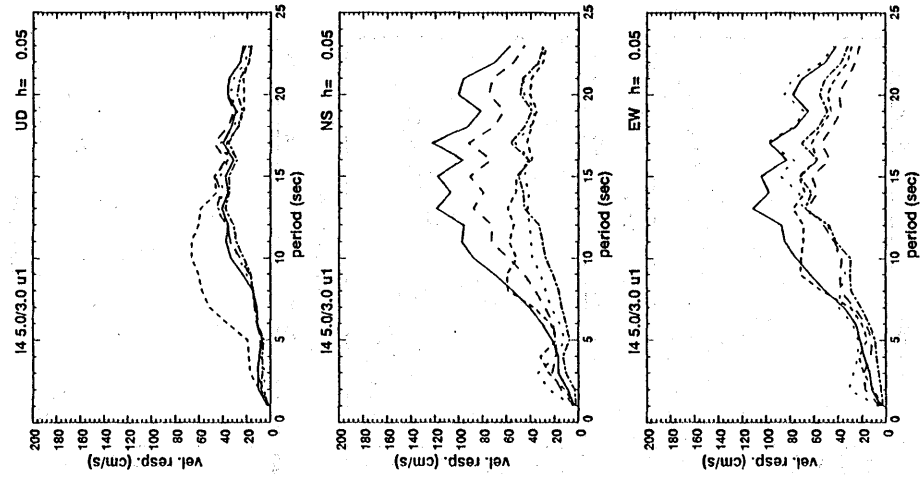
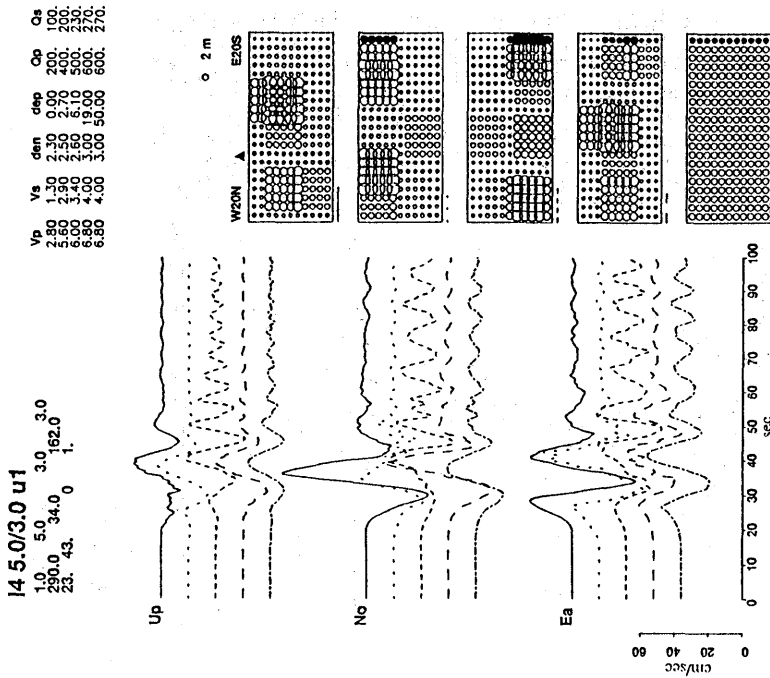
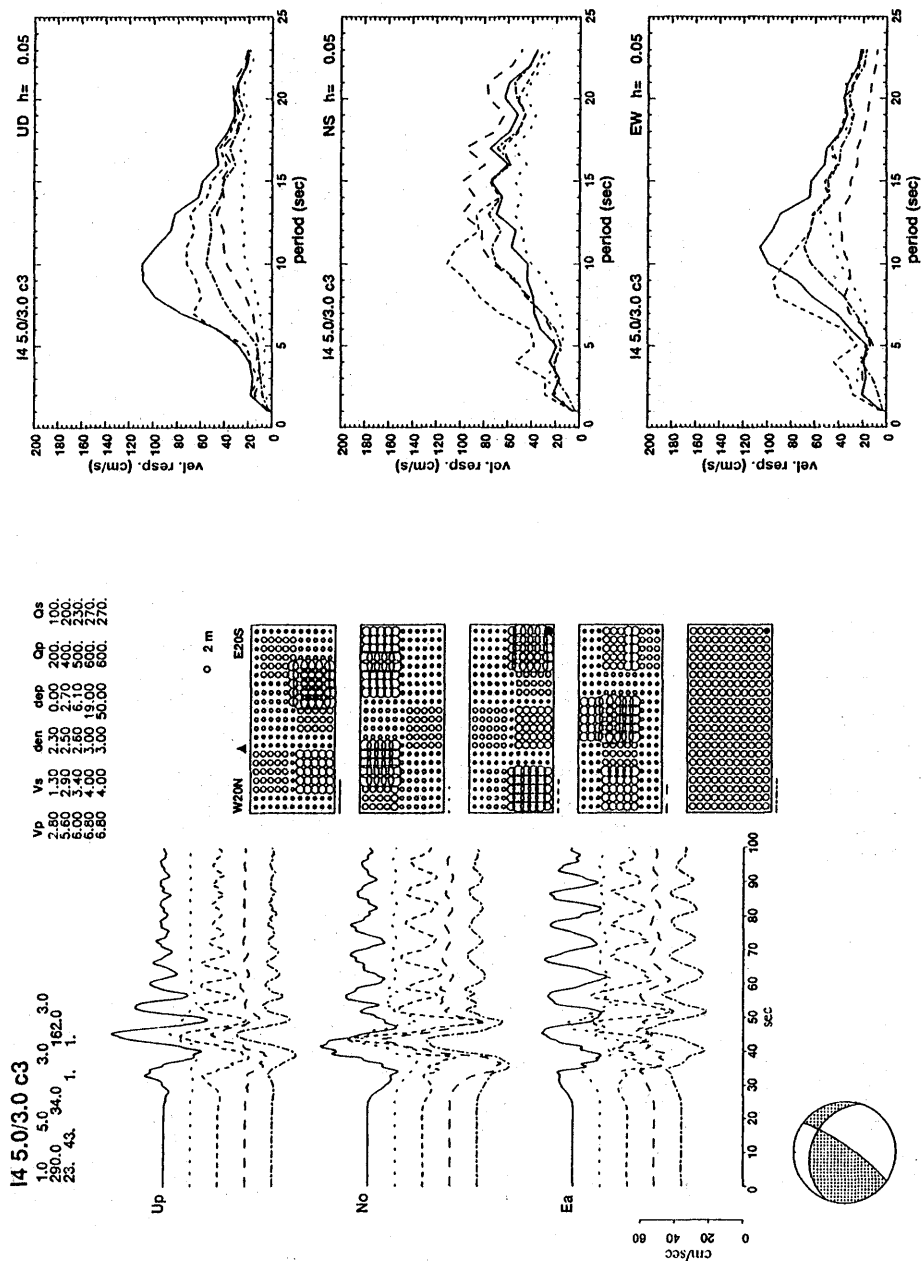


Fig. 15. Velocity response spectra (5% damping) of ground motions for the bilateral rupture case. IS structure in Table 3 is used in the calculation.

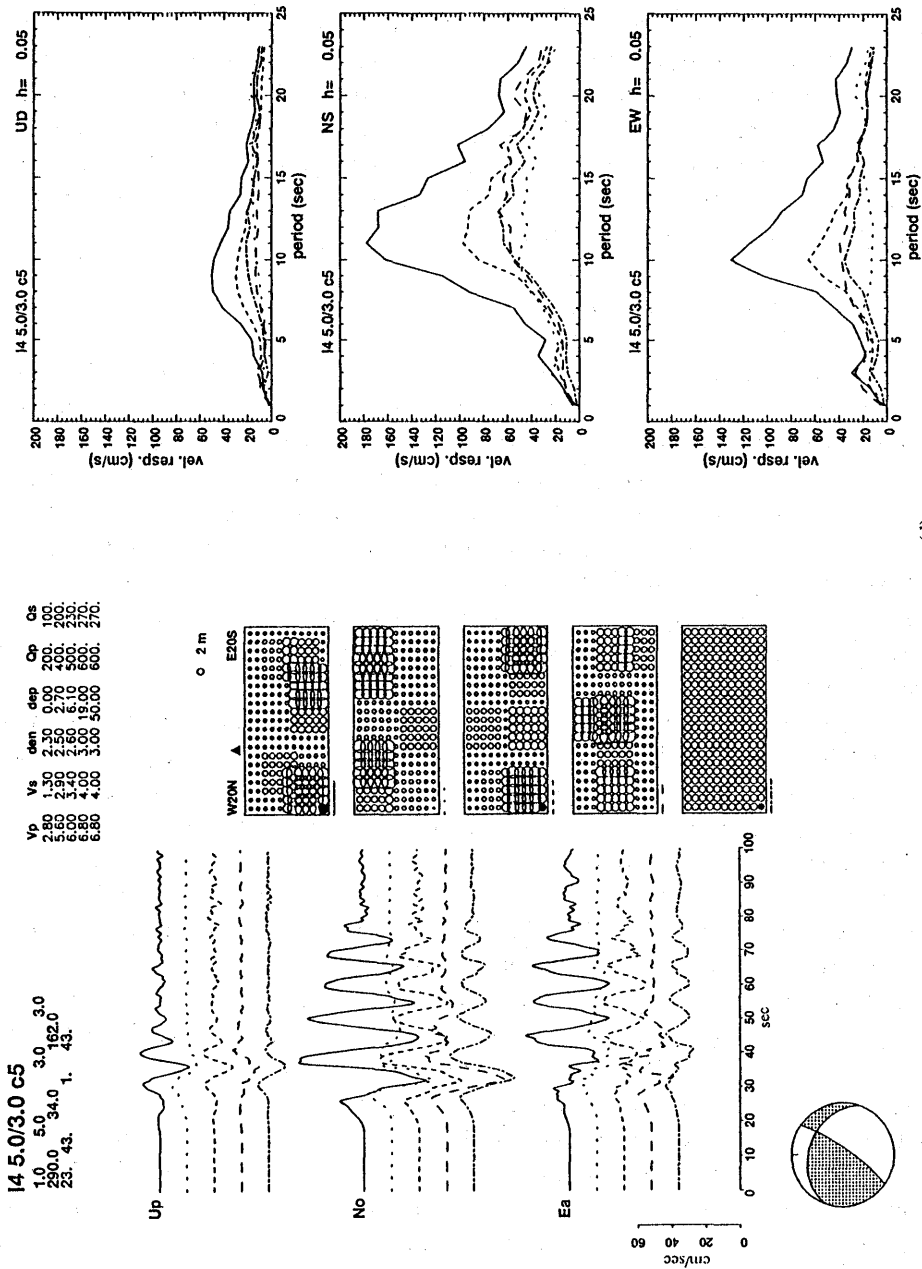


(b)





(c)



we performed several simulations using the velocity structure *15* listed in Table 3, and compared the results with those obtained above. Figure 15 shows the velocity response spectra (5% damping) for the bilateral case, with $v_r=3.0$ km/sec and $t_2=5$ sec. Comparing this figure with Figure 12a, we estimate that the amplification factor of the horizontal components is about 1.4 for the periods longer than 5 sec. This is almost equal to the amplification factor for a vertically incident *SH* wave at the sedimentary layer. The response spectra of the vertical component are, however, almost the same as those for the *14* case. Other rupture modes also give a similar amplification factor. For the ground motion with periods shorter than 5 sec, the amplification factor becomes as large as 2, because the reflection from the bottom of the sedimentary layer just beneath the station generates relatively large short-period waves.

Representative Ground Motion

Some representative ground-motion velocities are shown in Figure 16. The waveform at the top of each figure is the ground-motion velocity which gives the largest response spectrum among the particular rupture mode, and the bottom is that calculated for a homogeneous slip model. The middle three waveforms are for the following three extreme slip distributions on the fault: the largest subevent near the station site (the second trace), the largest subevent away from the site (the third trace), and the largest subevent at the center of the fault (the fourth trace). The corresponding slip distributions are shown on the right side of the waveforms, in the same order. The velocity response spectra (5% damping) are also shown at the right end of these figures. The line types of spectra correspond to those of the waveforms.

For the bilateral case (Figure 16a), the peak-to-peak amplitudes of the NS and the EW components reach 85 cm/sec and 75 cm/sec, respectively; however, the duration is less than 30 sec. A large vertical ground motion is excited for the *c3* rupture mode, and the peak-to-peak amplitude reaches 55 cm/sec (Figure 16c). This large vertical motion is caused by the large subevent located at the shallow eastern part of the fault, which produces a large vertical Rayleigh-wave motion due to rupture directivity. When the rupture velocity is reduced to less than 2 km/sec, the vertical component of ground velocity no longer yields a large amplitude.

The largest response spectrum among all the simulation results is shown at the top of Figure 16d. The spectrum and the peak-to-peak amplitude are about 170 cm/sec and 75 cm/sec, respectively. The typical periods of this strong motion are about 10 to 13 sec, and the duration is about 1 min. The large shallow subevent at the western end of the fault and the rupture directivity are responsible for this large amplitude. This ground motion is similar to that estimated from the Ewing seismogram (EV in Figure 3). When we reduce the rupture velocity to less than 1.5 km/sec, the peak-to-peak amplitude decreases to 18 cm/sec. Ground-motion velocities calculated using the different velocity structures are compared in Figure 17. The low-velocity surface layer is also responsible for this large motion, as shown in Figure 17.

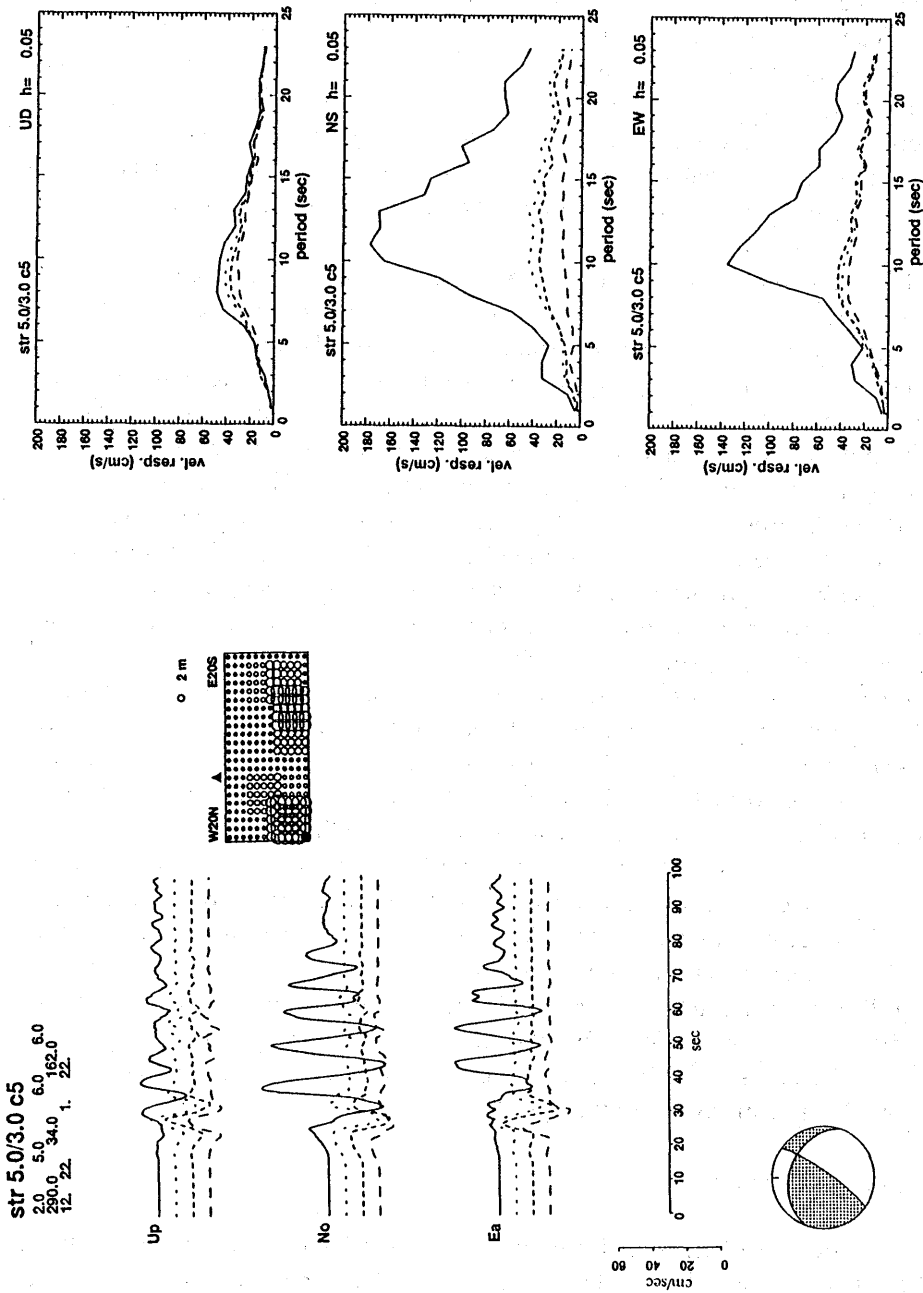


Fig. 17. Comparison of waveforms and response spectra (5% damping) calculated for the four different velocity structures listed in Table 1. The rupture propagation mode of c_5 is assumed in this calculation. The slip distribution on the fault plane is shown at the center.

Response Spectrum for the 1923 Kanto Earthquake

As shown above, our numerical simulations produce a wide range of ground motions and response spectra even for a given fault geometry and seismic moment.

The epicenter of the Kanto earthquake is located near the western end of the fault plane (Imamura, 1925; Kunitomi, 1930; Kanamori and Miyamura, 1970), which suggests that the rupture mode of either $c1$, $c5$, or $u2$ is probably appropriate. The response spectra for $c5$ have a range of 10 to 100 cm/sec at a period of 7.5 sec, which brackets the reference level. The response spectra for $c1$ and $u2$ are consistently smaller than those for $c5$. It is interesting to note that the epicenters suggested by all the authors listed above are close to the southwestern end of the fault plane and suggest that the $c5$ rupture mode is the most appropriate.

All the response spectra for the simulated ground motions computed for $c5$ have a peak at a period range of 10 to 13 sec, which is very similar to the velocity response spectrum estimated from the Ewing seismogram. The ground-motion velocity, response spectrum and the corresponding rupture pattern for several models are shown in Figure 18. The ground motions for the models shown may look too simple; however, they are indeed similar to the ground motion EV estimated from the Ewing seismogram.

In a basin filled with sedimentary layers, the waves trapped in the basin and surface waves converted from body waves at the edge of the basin exhibit a complex wave field (Vidale and Helmberger, 1988; Dreger and Helmberger, personal written communication). These waves produce large late surface waves and substantially increase the overall duration of ground motion. During the 1923 Kanto earthquake, the strong motion lasted for several minutes (Imamura, 1925), and the Imamura strong-motion seismogram (magnification: 2) was off-scale for more than 5 min. It is probable that this long reverberation is partly due to the shallow basin effects and partly due to the successive occurrence of large aftershocks. Since our simulations are made using 1-D structures, this basin effect is not included. The velocity record obtained by Yokota *et al.* (1989) from the Imamura seismogram indicates that the average amplitudes for the time intervals from 100 to 300 sec and 300 to 500 sec are about 1/2 and 1/5 of that of the first 100 sec, respectively. To examine the basin effect on the response spectrum, we took one of the representative ground motions with 100 sec duration and concatenated nine of them, with a 50 sec overlap between consecutive records, to produce a 500 sec long ground motion. Then we reduced the average amplitude of the portion from 100 to 300 sec and 300 to 500 sec to 1/2 and 1/5 of the first 100 sec, respectively, to simulate the lengthening effect of the basin. As shown in Figure 19, the response spectrum of this stretched record is essentially the same as that of the original.

Variability of the Spectrum

As mentioned earlier, future large earthquakes near Tokyo may be dissimilar to the 1923 Kanto earthquake, even if they share the same fault area and mechanism as that event. The sensitivity study suggests that the slip distribution, the rupture mode, rise time, rupture velocity, and the existence of a very soft layer can significantly change the ground-motion estimates and the spectra. Although the details are shown in Figures 12–

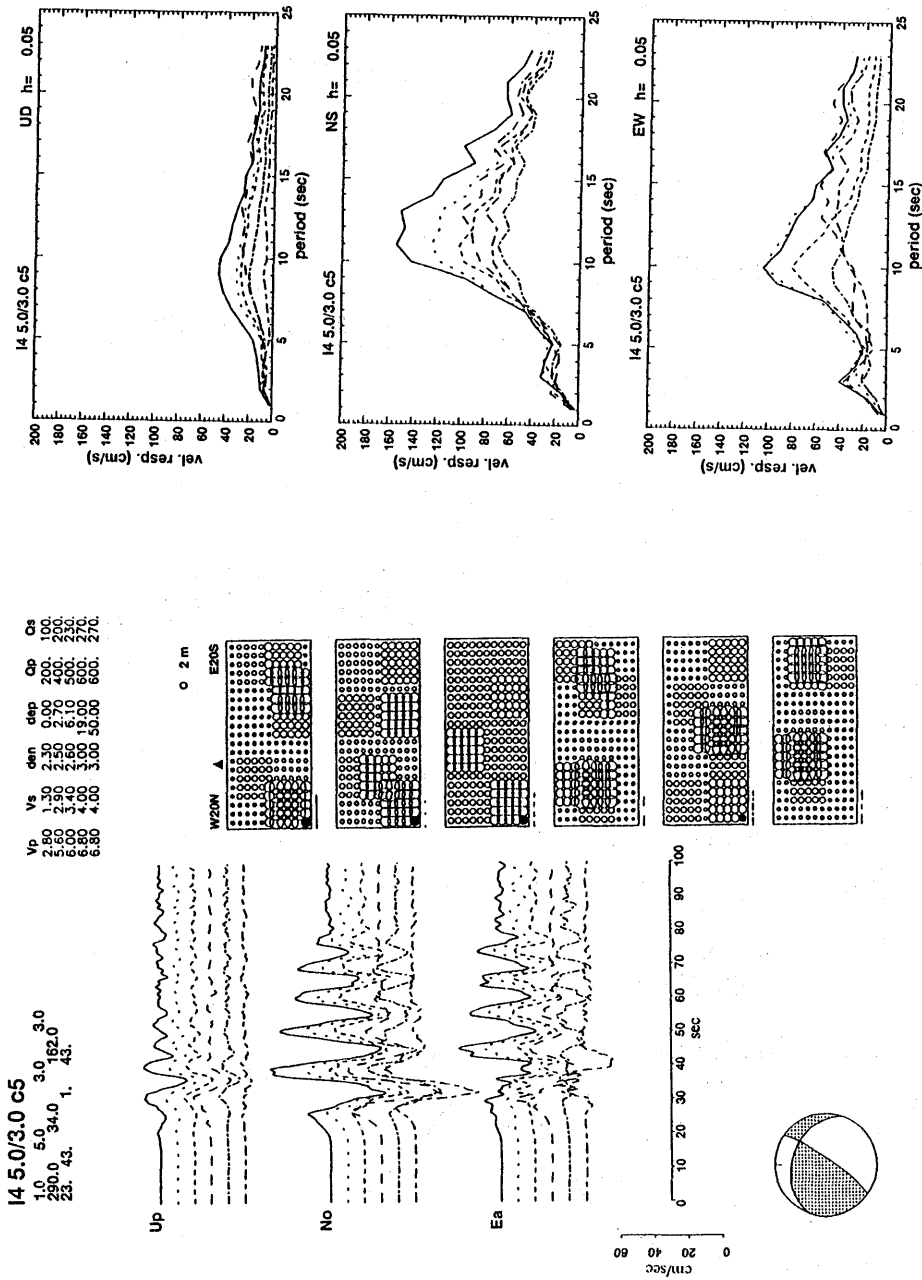


Fig. 18. Ground-motion velocity, response spectrum and the corresponding rupture pattern for several models computed for c5 rupture mode. All the spectra have a range of 40 to 60 cm/sec at a period of 7.5 sec.

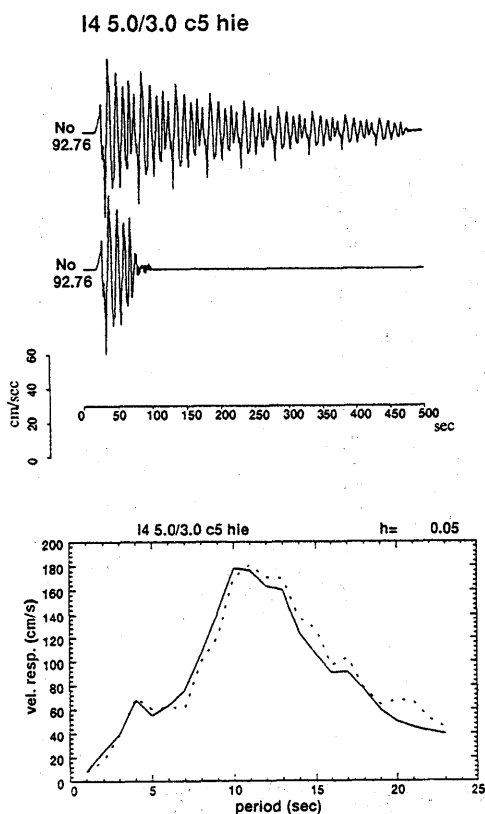


Fig. 19. A stretched ground motion (upper trace of the records) and its response spectrum (solid curve in the lower panel). The original ground motion (lower trace) and its response spectrum (dotted curve in the lower panel) are also shown.

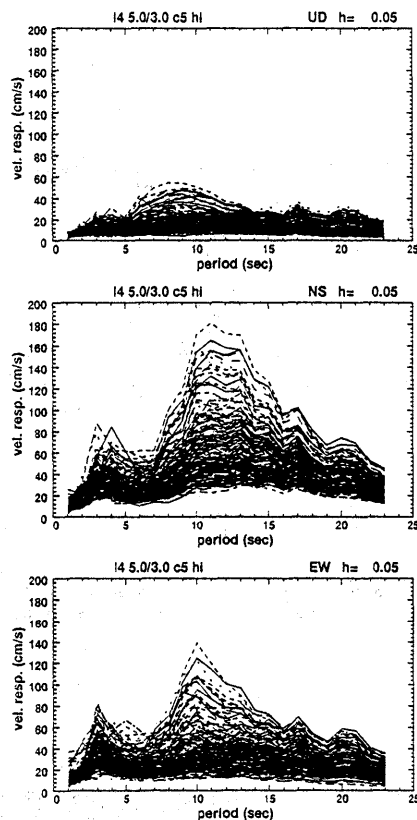


Fig. 21. Velocity response spectra (5% damping) of ground motions for the circular rupture mode of c5. I4 structure in Table 1 is used in the calculation. A hierarchical rupture process is assumed in the 3 km \times 3 km subfault.

Schematic velocity response spectra ($h=0.05$)

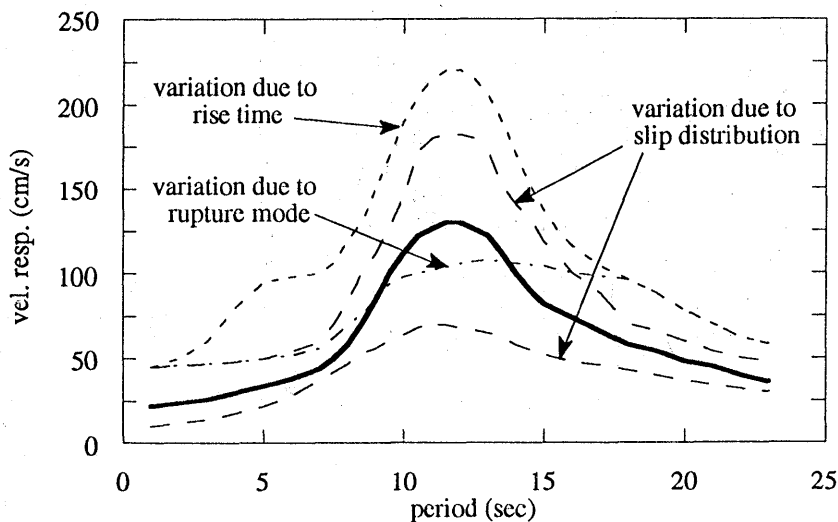


Fig. 20. Schematic illustration of variability of response spectrum.

15, we schematically show these effects in Figure 20.

In general, reducing the rise time or increasing the rupture velocity increases the spectral amplitude at periods shorter than 5 sec. Existence of large subevents in a shallow structure enhances the ground motion significantly, especially if it is combined with rupture propagation toward the site. Also, if the site is located on a very soft sediment, significant (a factor of 1.4) amplification occurs.

Discussion

For periods shorter than 5 sec, the simulated waveforms and the response spectra are strongly influenced by source-time function or dislocation rise time. The amplification of response spectra due to the change in the rise time t_2 from 5 to 3 sec is about 2 for periods shorter than 7 sec.

On the other hand, if we include small-scale roughness in the rupture process, the short-period response spectrum increases even if the gross rise time of dislocation remains constant. As an example, we employed a hierarchical model (Fukao and Furumoto, 1985; Kikuchi, 1989, 1991) for the rupture process. We assumed 9 small subevents in the 3 km \times 3 km subfault. The duration and the seismic moment of each subevent are 1/3 and 1/27 of those of the whole subfault, respectively. The response spectra at periods shorter than 5 sec increase by a factor of 2, but are about the same at longer periods. Figure 21 shows the response spectra using a hierarchical model with the *c5* rupture mode. A semi-empirical simulation of the 1923 Kanto earthquake by Niwa *et al.* (1992) gives velocity response spectra (5% damping) of several tens to 100 cm/sec at periods of 2 to 5 sec. The response spectra in these short periods are very strongly affected by the small-scale roughness, and deterministic estimation with numerical methods is difficult.

The epicenter of the 1923 Kanto earthquake is located near the western end of the fault plane (Imamura, 1925; Kunitomi, 1930; Kanamori and Miyamura, 1970). Although the depth is not well determined (Kanamori and Miyamura, 1970; Matsu'ura *et al.*, 1980; Hamada, 1987), the location of the epicenter suggests that the gross rupture propagation was similar to that of the *c5* rupture mode. In Figure 22, the ground-motion velocities reproduced from the Ewing seismogram and the Imamura seismogram are compared with the simulated ground-motion velocity for the *c5* rupture mode that yields the largest response spectrum. The response spectra of the horizontal components and the reproduced records are also shown in this figure. The period of 10 to 13 sec in which the peak of the synthetic horizontal components occurs is almost the same as the dominant period of the motion reproduced from the Ewing record. The slip distribution of this particular case has large slip of about 8 m in the shallow part of the western end of the fault plane. This large subevent and the rupture directivity cause the large long-period waveform. Even if the large subevents in Figure 22 are moved to deeper parts of the fault plane, where the upper edges of subevents are 8 km, the large long-period waveform still has a peak-to-peak amplitude of more than 60 cm/sec, and the response spectrum reaches 120 cm/sec at the period of 13 sec. When the depth of the hypocenter is 10 km and the rupture propagates circularly from there, the peak-to-peak amplitude

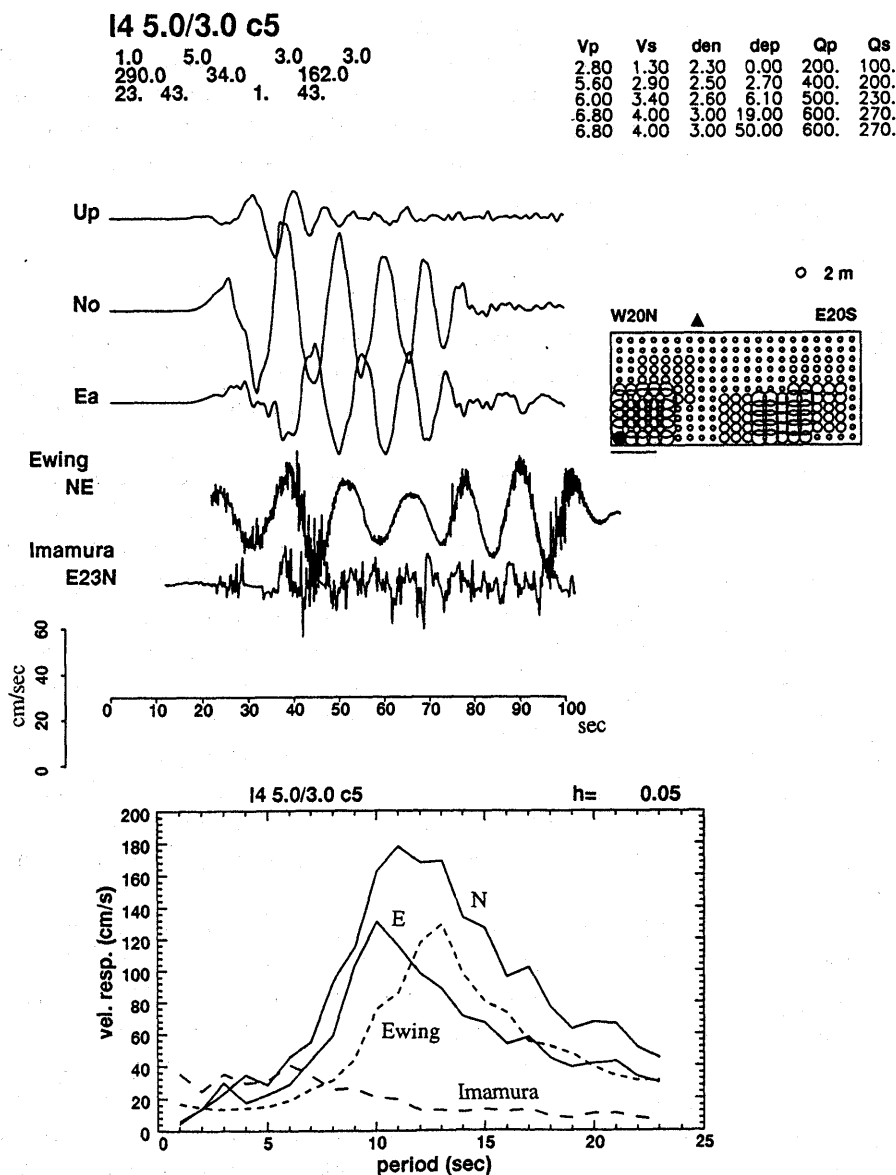


Fig. 22. Comparison of ground-motion velocities estimated from the Ewing seismogram and the Imamura seismogram with the simulated ground-motion velocity for $c5$ rupture mode which gives the largest response spectrum. The response spectra (5% damping) of the horizontal components and the estimated ground motions are shown in the lower panel of this figure.

and the response spectrum at the period of 13 sec are 55 cm/sec and 108 cm/sec, respectively. Thus, a slight difference in the depth would not significantly affect the excitation of long-period waves. Matsu'ura's fault model of the 1923 Kanto earthquake indicates large slip of 7.4 m on a subfault at the western end of the fault plane; the location and size of this subfault are similar to those of the large subevent of our model used for this simulation. This result suggests that this subfault is responsible for the large long-

period ground motion recorded in Tokyo during the 1923 Kanto earthquake.

The response spectra shown in Figure 22 peak at 10 to 13 sec, which is considerably longer than that for the Green's functions shown in Figure 6b. This suggests that the peak of the ground-motion spectra from large earthquakes does not necessarily coincide with that of the site response computed for a point source. Because of the rupture propagation over a large fault area, the site response may have to be significantly modified to estimate the ground-motion spectrum.

Conclusion

Although the low-gain seismograms recorded in Tokyo during the 1923 Kanto earthquake are unique, the difficulty in restoring the clipped portion of the Imamura seismogram and in removing the instrument response from the Ewing seismogram made it difficult to definitively determine the ground motions during the earthquake. We re-examined the Ewing seismogram and concluded that the large ground motion with a period of about 13 sec estimated by Morioka (1976, 1980) is real. Also, the most probable value of the velocity response spectrum of the horizontal ground motion is about 50 cm/sec at a period of 7.5 sec. Our simulations produced a wide range of ground motions and response spectra, even with a given fault geometry and seismic moment. For a rupture model which initiates from the southwestern end of the fault plane, the most probable epicenter of the 1923 earthquake, the computed response spectra have a range of 10 to 100 cm/sec at a period of 7.5 sec, which brackets the observed level. All the response spectra computed for this model have a peak in a period range of 10 to 13 sec which is different from that of the site response.

The differences in the slip distribution and the rupture direction cause the large variation in the simulated ground motion. Large subevents in a shallow structure enhance the ground motion significantly, especially if the rupture propagation is toward the site. One of our extreme models, which has large slip of about 8 m in the shallow part of the western end of the fault plane, can produce a large ground motion similar to that estimated by Morioka (1976, 1980). Reducing the rise time or increasing the rupture velocity increases the spectral amplitude at periods shorter than 5 sec. Also, if the site is located on a very soft sediment, significant (a factor of 1.4) amplification occurs.

Although our simulations are made for models of the 1923 Kanto earthquake, there is no reason to believe that the next large earthquake near Tokyo will be similar to the 1923 Kanto earthquake. Many earthquake sequences along subduction zones demonstrate that earthquakes are very noncharacteristic from sequence to sequence. It is thus important to consider for various design purposes the variability of ground motions caused by changes in the model parameters.

Acknowledgments

We thank H. Yokota and S. Kataoka, Institute of Technology, Shimizu Co., who kindly provided us with the digitized ground-motion data reproduced from the Imamura seismogram; and M. Yamada, Waseda University, who kindly provided us with the

digitized ground-motion data reproduced from the Ewing seismogram. M. Takeo was supported under the visitor program of the Southern California Earthquake Center and the exchange visitors program of the Ministry of Education, Science and Culture, Japan. This research was partially supported by the CUREe-Kajima Research Project. We have greatly benefitted from interaction with the Kajima research group on this subject. In particular, discussions with Drs. M. Niwa, M. Motosaka, M. Takemura, and H. Yamanaka have been very helpful during the course of this study. Contribution No. 5192, Division of Geology and Planetary Sciences, California Institute of Technology, Pasadena, California 91125.

Appendix

Comparison of the Ground Motions Estimated from the Ewing and the Imamura Seismograms.

The ground-motion displacement estimated by Yokota *et al.* (1989) from the clipped Imamura seismogram (IMD, IMV) and that by Morioka (1976, 1980) from the Ewing seismogram (ED, EV) are significantly different, as shown in Figure 3. We investigated this difference with the hope of obtaining a consistent estimate of long-period response spectrum for the 1923 Kanto earthquake.

Ewing Seismogram

Since the original Ewing seismogram traced by Nasu (1971b) clearly shows very large long-period waves (Figure 2a), it is hard to deny that the ground motion of the Kanto earthquake had very large long-period components. However, a very unusual characteristic of this seismogram is that it is almost sinusoidal, with a sharp spectral peak at 13 sec. Probably because of this peculiar feature, this seismogram has not received much attention.

The Ewing seismograph has a natural period of 6 sec, with a very weak damping of 4.5% (Nasu, 1971b, Morioka, 1976), which causes its response to have a sharp peak at 6 sec; at this period the magnification is about 11 times the static magnification, 1. If the short-period (about 5 sec) waves seen in IMD (Figure 3) are real, it is very strange that the Ewing seismogram did not show any indication of a spectral peak at 6 sec. One possibility is that the strong shaking shifted the natural period of the Ewing seismogram to 13 sec. However, this is unlikely because it is in general difficult to maintain a stable long-period response of a horizontal pendulum. If the strong shaking had any effect on the instrument, it would have shortened the period, or would have thrown the pendulum off-balance. The Ewing seismogram does not show any sign of such instability.

In the following, we consider several possibilities for explaining this peculiar feature.

1) Rotation rate of the recording disk.

One possibility is that the rotation rate of the recording disk of the Ewing seismograph was faster than that (3°/sec) assumed by Morioka (1976). If it was faster by a factor

of 2, then the period of the seismogram was actually 6.5 sec instead of 13 sec. This is, however, unlikely, because the record of an aftershock on January 14, 1924 ($M=7.3$) did show oscillations at about 6 sec (Nasu, 1971b), with the assumption that the rotation rate was $3^\circ/\text{sec}$.

2) Lengthening of the natural period due to large amplitude.

The ground motion during the Kanto earthquake was about 50 cm on the recording disk of the Ewing seismograph. Since the pendulum length of the Ewing seismograph is about 50 cm, the ordinary small amplitude approximation for the simple pendulum may not be valid. The exact solution for a simple pendulum with a finite amplitude can be written as

$$\sin(\phi/2) = k \operatorname{sn}(\sqrt{g/l} t, k), \quad k = \sin(\alpha/2)$$

where t , ϕ , g , l and α are the time, the angle from the vertical, the acceleration of gravity, the pendulum length, and the maximum oscillation angle, respectively. The function $\operatorname{sn}(x, k)$ is the Legendre-Jacobi elliptic function of the first kind. Then the period of the pendulum is given by

$$T = 4\sqrt{l/g} K(k) = (2/\pi) K(k) T_0, \quad T_0 = 2\pi\sqrt{l/g}$$

where $K(k)$ is the Legendre-Jacobi elliptic integral of the first kind, and T_0 is the period of the pendulum for an infinitesimal amplitude. For a maximum angle of 40° , $\alpha=0.70$, $k=0.34$, and $K(k)=1.62$, which yields $T/T_0=1.03$. Thus, the change in the period is only 3%, even for the very large amplitude of 40° , and is not large enough to explain the unusual behavior of the Ewing seismograph during the Kanto earthquake.

3) The effect of tilt.

Ground tilting causes a change in the natural period of a horizontal pendulum. If we let T and θ be the period and the tilt of the pendulum axis from the vertical, respectively, then

$$dT/d\theta = T/2\theta$$

Since $T=6$ sec, and $\theta=0.058$ radian ($=3.3^\circ$) for the Ewing seismograph, $dT/d\theta=50$. Since the maximum tilt during the Kanto earthquake was probably 3×10^{-4} , the change in the period is considered negligible.

4) Solid friction.

The equation of a simple pendulum with solid friction is given by,

$$\ddot{x} + 2\varepsilon\omega_0\dot{x} + \omega_0^2(x + \operatorname{sign}(\dot{x})r) = -V\ddot{y} \quad (\text{A1})$$

where x is the linear response of the seismograph, y is the ground motion, ε is the damping constant, ω_0 is the natural angular frequency of the pendulum, V is the static magnification, and r is the solid friction. The solid friction r gives the range of the "dead zone" of the pendulum around the equilibrium point. Because of the $\operatorname{sign}(\dot{x})$ term equation A1 is

nonlinear, and its solution exhibits very unexpected behavior. When the ground motion y is simple harmonic, the seismograph response is not very different from the ordinary damped harmonic motion. However, if the ground motion consists of more than one harmonic component, the response becomes very unpredictable. Figure A1 illustrates this situation, which simulates the Ewing seismograph with solid friction. The seismograph pendulum period T_0 , damping constant ϵ , and the friction r , are 6 sec, 0.045, and 10 cm respectively. The ground motion is given by.

$$y(t) = a_1 \sin(2\pi t/T_1) + a_2 \sin(2\pi t/T_2)$$

where $T_1=13$ sec, $T_2=6$ sec, $a_1=60$ cm, and $a_2=12$ cm. The upper two traces in Figure A1a show the response with and without solid friction, and Figure A1b shows the corresponding spectra. Since T_2 is the same as T_0 and the damping is very small (4.5%), the response without solid friction is sharply peaked at 6 sec. However, with solid friction, this peak is almost completely suppressed, but the long-period peak is not significantly modified from the frictionless case. Because of the nonlinear behavior, it is not obvious exactly how this occurs, but the solid friction in the system damps out the short-period motion, and the overall response is controlled by the larger amplitude long-period ground motion. Thus, the unusual waveform of the Ewing seismogram with no spectral peak at the resonance period could be explained if the solid friction was relatively high during shaking. Although there is no way of proving this, we suspect that the friction could have become very large when the straw stylus was driven violently on

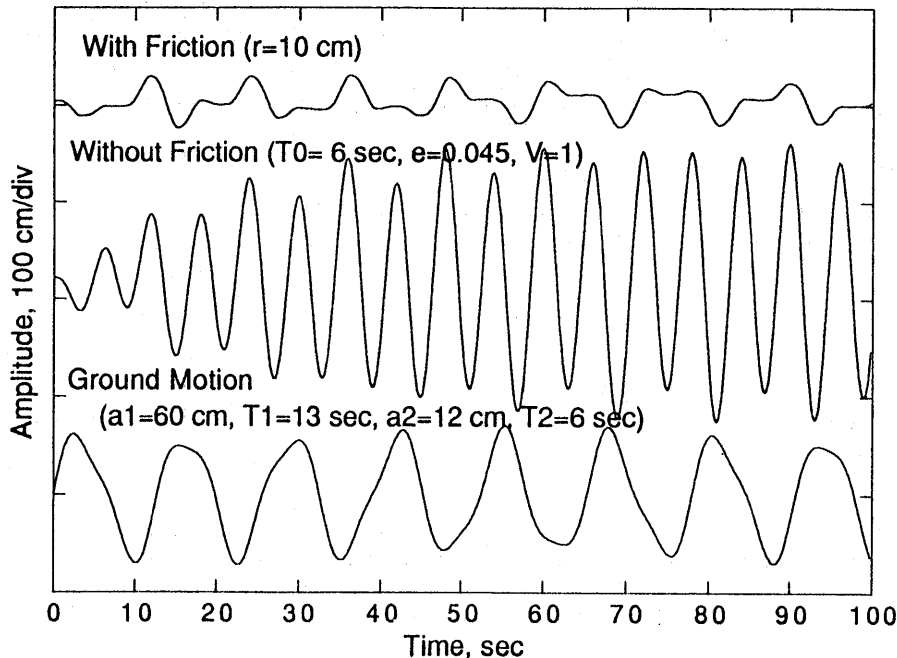


Fig. A1(a)

Fig. A1. Simulation of a Ewing seismograph with solid friction. The seismograph pendulum period T_0 , damping constant ϵ , and the friction r , are 6 sec, 0.045, and 10 cm, respectively. (a). The upper and middle traces show the responses with and without solid friction, respectively. The bottom trace is the input ground motion used in this simulation. (b). The corresponding Fourier spectra of the responses and the input ground motion.

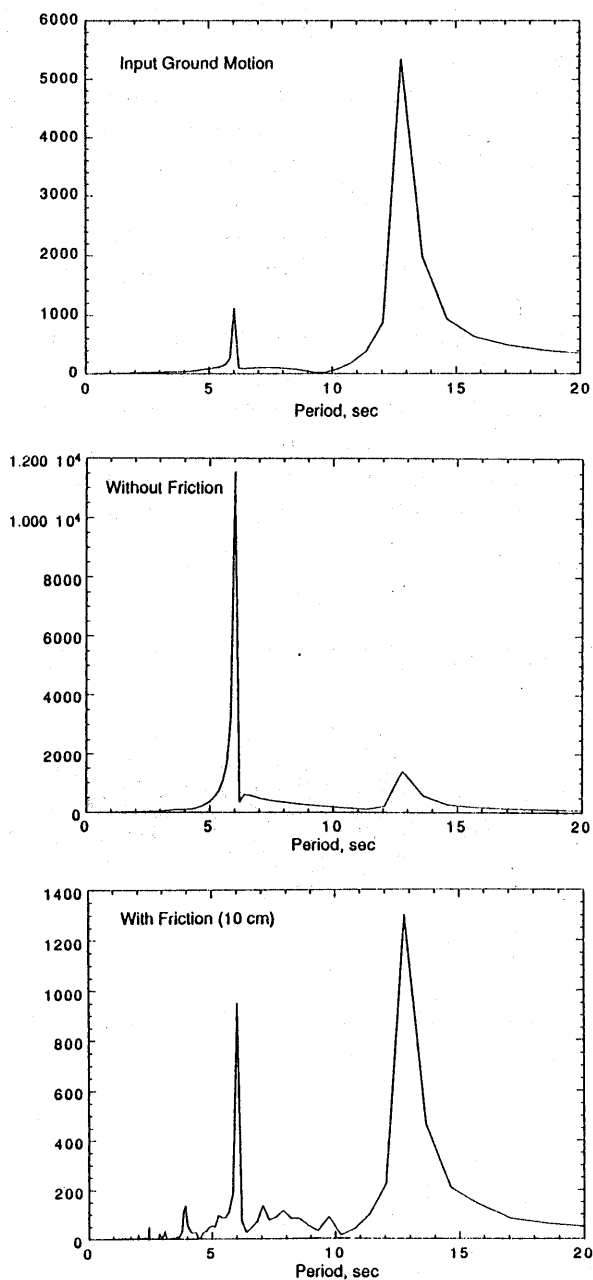


Fig. A1(b)

the disk, occasionally off the disk, and was consequently partly worn down. The Ewing seismograph has a relatively small mass (2.5 kg) and is more sensitive to solid friction between the recording stylus and the disk. If this interpretation is correct, the long-period ground motion recorded on the Ewing seismograph must be real, and the spectral amplitude for the long-period motion estimated from it using the response without

friction should be approximately correct. However, the spectral amplitude at periods less than 10 sec is probably grossly underestimated.

Since the problem is nonlinear, the exact response depends on the input waveform and amplitude. To investigate a more realistic case, we used a synthetic ground motion (acceleration) shown in Figure A2 as the input ground motion. As shown in Figure A2, this ground motion has a fairly smooth spectrum over a period range from 5 to 20 sec. Figure A3 shows the Ewing seismograms for this ground motion for the case with and without friction. Without friction, the spectrum is sharply peaked at 6 sec, but, when friction is added, the peak is suppressed and the seismogram resembles the Ewing seismogram observed for the Kanto earthquake. The spectral amplitude at long period (>8 sec) for the case with friction is about the same as that without friction, suggesting that the long-period ground motion estimated from the observed Ewing seismogram is a good approximation of the real ground motion.

From these numerical experiments, we believe that the ground motion estimated by Morioka (1976, 1980) represents the real long-period ground motion during the Kanto earthquake.

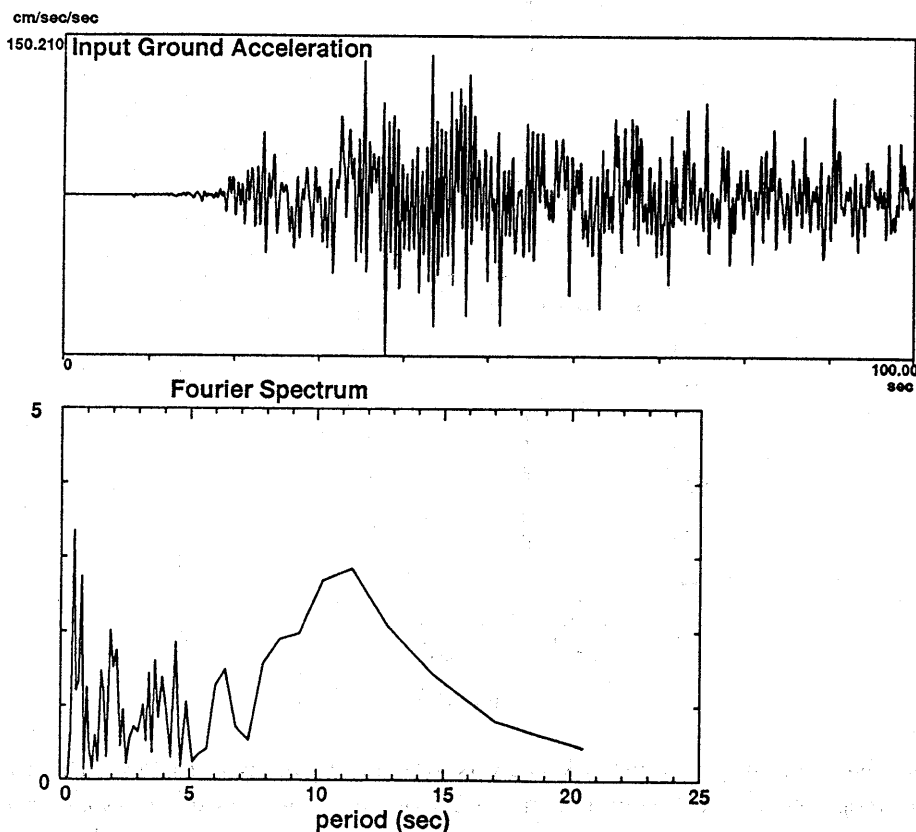


Fig. A2. Input synthetic ground motion (acceleration) used in a more realistic simulation. The Fourier spectrum is shown in the lower panel.

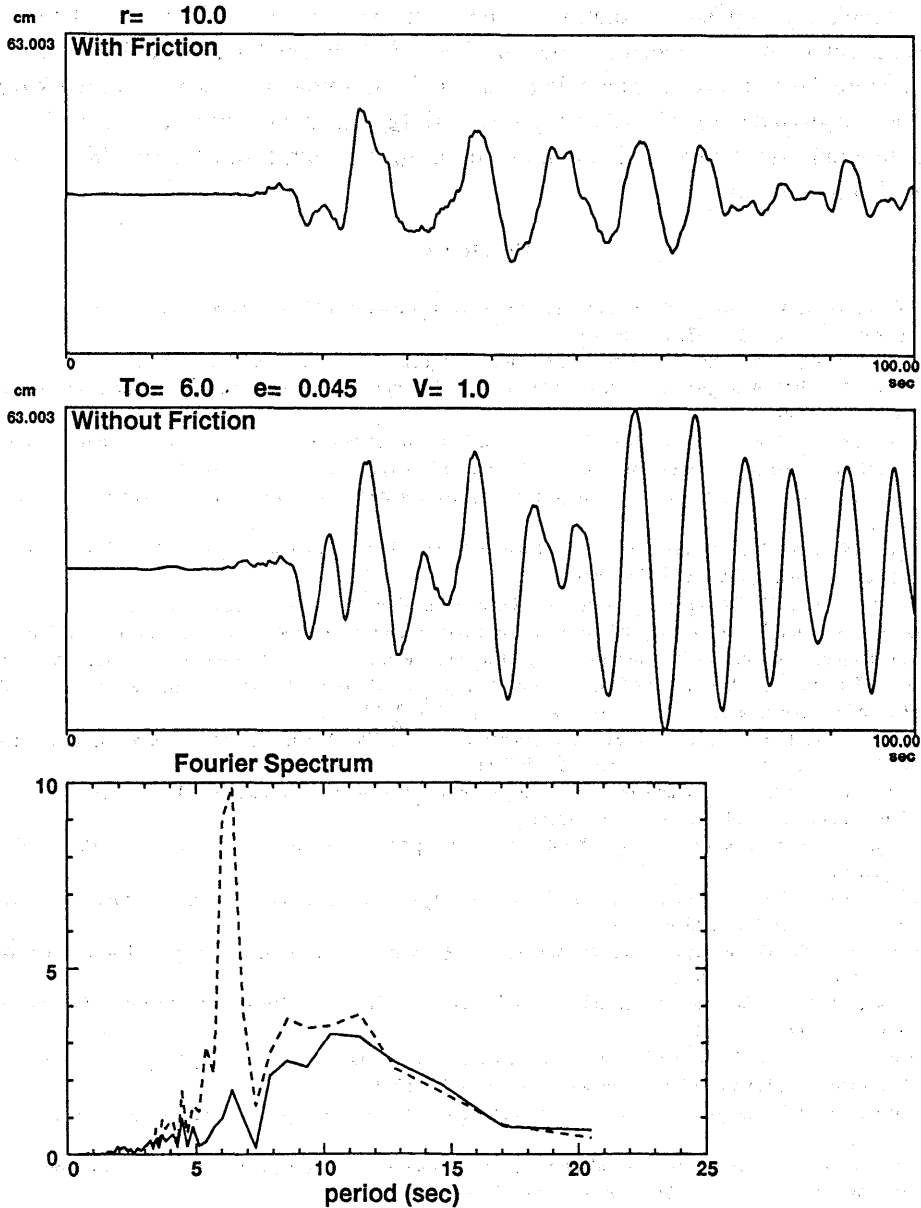


Fig. A3. Responses of the Ewing seismograph with and without solid friction for a more realistic input ground motion. Fourier spectra of these responses are shown by solid curve (with solid friction) and dotted curve (without solid friction).

Imamura Seismogram

The Imamura seismograph recorded the ground motions of the Kanto earthquake on-scal for the first 15 sec, but went off-scale thereafter for about 5 min (Figure 2b). Yokota *et al.* (1989) developed a method to restore the clipped portion of the record with the assumption that the damper plate collided against the stopper. Since the seismogram

is completely clipped, restoration is inevitably very difficult. The ground motion displacement thus estimated is shown in Figure 3. Although their method may be able to restore the motions which are dominant on the seismogram, it would not work well if the real ground motion had the very long-period component estimated from the Ewing seismogram. As shown in Figure 3, the response spectrum computed for IMD is very small at long period.

References

- ANDO, M., 1971, A fault-origin model of the great Kanto earthquake of 1923 as deduced from geodetic data, *Bull. Earthq. Res. Inst., Univ. Tokyo*, **49**, 19–32.
- ANDO, M., 1974, Seismo-tectonics of the 1923 Kanto earthquake, *J. Phys. Earth*, **22**, 263–277.
- BOUCHON, M., 1981, A simple method to calculate Green's functions for elastic layered media, *Bull. Seismol. Soc. Am.*, **71**, 959–971.
- COHEE, B.P., P.G. SOMERVILLE and N.A. ABRAHAMSON, 1991, Simulated ground motions for hypothesized Mw=8 subduction earthquakes in Washington and Oregon, *Bull. Seismol. Soc. Am.*, **81**, 1–29.
- FUKAO, Y. and M. FURUMOTO, 1985, Hierarchy in earthquake size distribution, *Phys. Earth Planet. Inter.*, **37**, 149–168.
- HAMADA, N., 1987, Note on the focal depth of the 1923 great Kanto earthquake, *Quarterly J. Seismol., Japan Meteorol. Agency*, **50**, 1–6 (in Japanese).
- HARTZELL, S.H., 1978, Earthquake aftershocks as Green's functions, *Geophys. Res. Lett.*, **5**, 1–4.
- HARTZELL, S.H. and T.H. HEATON, 1983, Inversion of strong ground motion and teleseismic waveform data for the fault rupture history of the 1979 Imperial Valley, California, earthquake, *Bull. Seismol. Soc. Am.*, **73**, 1553–1583.
- HEATON, T.H. and S.H. HARTZELL, 1989, Estimation of strong ground motions from hypothetical earthquakes on the Cascadia subduction zone, Pacific Northwest, *Pageoph*, **129**, 131–201.
- HOUSTON, H. and H. KANAMORI, 1986, Source characteristics of the 1985 Michoacan, Mexico earthquake at periods of 1 to 30 seconds, *Geophys. Res. Lett.*, **13**, 597–600.
- HOUSTON, H., 1987, Source characteristics of large earthquakes at short periods, Ph. D. Dissertation, 129p., California Institute of Technology, Pasadena.
- IMAMURA, A., 1925, Report on the great Kanto earthquake, *Rep. Imp. Earthq. Invest. Comm.*, **100A**, 21–65 (in Japanese).
- IRIKURA, K., 1983, Semi-empirical estimation of strong ground motions during large earthquakes, *Bull. Disas. Prev. Res. Inst., Kyoto Univ.*, **33**, 63–104.
- ISHIBASHI, K., 1985, Possibility of a large earthquake near Odawara, central Japan, preceding the Tokai earthquake, *Earthq. Pred. Res.*, **3**, 319–344.
- KANAMORI, H., 1971a, Faulting of the great Kanto earthquake of 1923 as revealed by seismological data, *Bull. Earthq. Res. Inst., Univ. Tokyo*, **49**, 13–18.
- KANAMORI, H., 1971b, Focal mechanism of the Tokachi-Oki earthquake of May 16, 1968: Contortion of the lithosphere at a junction of two trenches, *Tectonophysics*, **12**, 1–13.
- KANAMORI, H., 1974, Long-period ground motion in the epicentral area of major earthquakes, *Tectonophysics*, **21**, 341–356.
- KANAMORI, H., 1979, A semi-empirical approach to prediction of long-period ground motions from great earthquakes, *Bull. Seismol. Soc. Am.*, **69**, 1645–1670.
- KANAMORI, H. and S. MIYAMURA, 1970, Seismological re-evaluation of the great Kanto earthquake of September 1, 1923, *Bull. Earthq. Res. Inst., Univ. Tokyo*, **48**, 115–125.
- KANAMORI, H., P.C. JENNINGS, S.K. SINGH, E. MENA and L. ASTIZ, 1992, Estimation of strong ground motions in Mexico City expected for large earthquakes in the Guerrero seismic gap, submitted to *Bull. Seismol. Soc. Am.*.
- KENNETT, L.N. and N.J. KERRY, 1979, Seismic waves in a stratified half-space, *Geophys. J.R. Astron. Soc.*, **57**, 557–583.
- KIKUCHI, M. and Y. FUKAO, 1987, Inversion of long-period P-waves from great earthquakes along subduction zones, *Tectonophysics*, **144**, 231–247.
- KIKUCHI, M., 1989, Hierarchy model of an earthquake source process, *Special Rep. Natural Disas. Sci.*, No. **62601022**, 44–58 (in Japanese).
- KIKUCHI, M., 1991, Source-time-function of a hierarchy model, *Special Rep. Natural Disas. Sci.*, No. **01601033**, 155–162 (in Japanese).

- MATSU'URA, M., T. IWASAKI, Y. SUZUKI and R. SATO, 1980, Statical and dynamical study on faulting mechanism of the 1923 Kanto earthquake, *J. Phys. Earth*, **28**, 119–143.
- KUDO, K., 1980, A study on the contribution of surface waves to strong ground motions, *Proc. 7th World Conf. Earthq. Eng.*, 499–506.
- KUNITOMI, S.I., 1930, Seismometrical study of the great Kwanto earthquake occurred on September 1st, 1923, *Geophysical Magazine*, **3**, 149–164.
- MENDOZA, C. and S.H. HARTZELL, 1988, Aftershock patterns and main shock faulting, *Bull. Seismol. Soc. Am.*, **78**, 1438–1449.
- MENDOZA, C. and S.H. HARTZELL, 1989, Slip distribution of the 19 September 1985 Michoacan, Mexico, earthquake: near-source and teleseismic constraints, *Bull. Seismol. Soc. Am.*, **79**, 655–669.
- MORI, J. and K. SHIMAZAKI, 1985, Inversion of intermediate-period Rayleigh waves for source characteristics of the 1968 Tokachi-Oki earthquake, *J. Geophys. Res.*, **90**, 11374–11382.
- MORIOKA, T., 1976, Ground motion of the 1923 Kanto earthquake, *Proc. 4th Symposium on Ground Motions, Architectural Inst. Japan*, 38–48 (in Japanese).
- MORIOKA, T., 1980, The ground motion of the great Kwanto earthquake of 1923, *Transactions of Architectural Inst. Japan*, **289**, 79–88.
- MORIOKA, T. and M. YAMADA, 1986, An attempt to estimate the maximum ground motion of the great Kanto earthquake of 1923, *Proc. 7th Symposium Japanese Earthq. Eng.*, 109–114.
- NASU, N., 1971a, Extremely strong ground motion 1, *Architectural Eng.*, No. 4, 123–127 (in Japanese).
- NASU, N., 1971b, Extremely strong ground motion 2, *Architectural Eng.*, No. 5, 123–134 (in Japanese).
- NIWA, M., T. OHTA, T. IKEURA, S. OHNO, T. NOZAWA and M. TAKEMURA, 1992, Ground motion study by fault model for tall building design, *Proc. 10th World Conf. Earthq. Eng.* (in press).
- OKAMOTO, T., Z. YAMADA and S. NODA, 1988, Estimation of sloshing height in the epicentral area of a hypothetical south Kanto earthquake, *Trans. Struct. Eng.*, **34A**, 961–972 (in Japanese).
- RESEARCH GROUP ON UNDERGROUND STRUCTURE IN THE TOKYO METROPOLITAN AREA, 1989, *Technical report on the Yumenoshima seismic refraction experiment*, 277p. (in Japanese).
- SHIMA, E., M. YANAGISAWA, K. KUDO, T. YOSHII, Y. ICHINOSE, K. SEO, K. YAMAZAKI, N. OHBO, Y. YAMAMOTO, Y. OGUCHI and M. NAGANO, 1976, On the base rock of Tokyo, *Bull. Earthq. Res. Inst., Univ. Tokyo*, **51**, 1–11 (in Japanese).
- SOMERVILLE, P.G., M. SEN and B. COHEE, 1991, Simulation of strong ground motions recorded during the 1985 Michoacan, Mexico and Valparaiso, Chile earthquakes, *Bull. Seismol. Soc. Am.*, **81**, 1–27.
- TAKEMURA, M. and T. IKEURA, 1987, Semi-empirical synthesis of strong ground motions for the description of inhomogeneous faulting, *Zisin*, **40**, 77–88 (in Japanese).
- TAKEO, M., 1985, Near-field synthetic seismograms taking into account the effects of anelasticity, *Meteorol. Geophys.*, **36**, 245–257 (in Japanese).
- TAKEO, M., 1988, Rupture process of the 1980 Izu-Hanto-Toho-Oki earthquake deduced from strong motion seismograms, *Bull. Seismol. Soc. Am.*, **78**, 1074–1091.
- TAKEO, M. and N. MIKAMI, 1990, Fault heterogeneity of inland earthquakes in Japan, *Bull. Earthq. Res. Inst., Univ. Tokyo*, **65**, 541–569.
- TAKEO, M., 1992, The rupture process of the 1989 Offshore Ito earthquakes preceding a submarine volcanic eruption, *J. Geophys. Res.*, **97**, 6613–6627.
- VIDALE, J.E. and D.V. HELMBERGER, 1988, Elastic finite-difference modeling of the 1971 San Fernando, California earthquake, *Bull. Seismol. Soc. Am.*, **78**, 122–141.
- WALD, D.J., L.J. BURDICK and P.G. SOMERVILLE, 1988, Simulation of acceleration time histories close to large earthquakes, *Proc. Earthq. Eng. Soil Dynamics 2nd Conference, Am. Soc. Civil Engineers, Geotechnical Special Publication*, No. 20, 430–444.
- WALD, D.J., D.V. HELMBERGER and T.H. HEATON, 1991, Rupture model of the 1989 Loma Prieta earthquake from the inversion of strong-motion and broadband teleseismic data, *Bull. Seismol. Soc. Am.*, **81**, 1540–1572.
- YAMANAKA, H., 1991, Analysis and modeling of long-period ground motion in the Kanto plain, Japan, *Proc. 4th International Conf. Seismic Zonation*, 75–82.
- YOKOTA, H., S. KATAOKA and T. TANAKA, 1989, Estimation of long-period ground motion of the 1923 great Kanto earthquake, *J. Struct. Constr. Eng., Architectural Inst. Japan*, No. 401, 35–45 (in Japanese).
- YOKOTA, H., 1991, A study on characteristics of input earthquake motions in Tokyo, *Special Rep. Inst. Tech., Shimizu Co.*, No. 33, 159p. (in Japanese).

1923 年関東地震 ($M \approx 8$) の長周期地震動

武 尾 実・金 森 博 雄

カリフォルニア工科大学

1923 年関東地震 ($M_s = 7.9 \sim 8.1$) の際の東京での長周期地震動の数値シミュレーションを行なった。地動の計算には、水平成層構造を仮定して反射・透過行列と離散化波数積分法を用いている。この論文の目的は以下の 2 点に要約される。1) 1923 年関東地震時の長周期地震動の応答スペクトルを見積もること、2) 種々の震源パラメータが地動に及ぼす影響を調べ、見積もられた地動の変動範囲を評価することにより、シミュレーションの結果をより一般的な地震に適用出来るようにすること。

1923 年関東地震の東京での地動は今村式強震計と Ewing 強震計に記録されている。これまでの研究では、これら 2 つの記録から推定された地動は非常に異なっていたが、我々は Ewing 強震計の摩擦抵抗がこの地震を記録しているときに大きかったと考えることにより、この矛盾を解決した。関東地震の際の東京での地震は大きな長周期成分を含んでおり速度応答スペクトル (5% damping) は周期 13 秒で 120cm/sec に達するものと考えられる。また、周期 7.5 秒付近での速度応答スペクトルは約 50cm/sec と見積もられる。

数値シミュレーションによる推定地動は一定の断層面と地震モーメントを与えた場合でも非常に大きく変化する。断層面上のすべり分布と破壊伝播の様式が推定地動に大きく影響する。1923 年関東地震と同様の破壊伝播を考えた場合でも、すべり分布の違いにより東京での速度応答スペクトル (周期 7.5 秒) は 10cm/sec から 100cm/sec まで変化する。一方、この破壊伝播の場合には、すべての速度応答スペクトルが周期 10 秒から 13 秒のところにピークを持つ形をしている。地殻浅部に大きなすべりがある場合、破壊伝播の効果が相乗すると大きな長周期地動が生成される。1923 年関東地震では、断層面の南西端付近の地殻浅部で約 8m のすべりが起こっていると、Ewing 強震計の記録から推定された大きな長周期地動に匹敵する地動がシミュレートされる。

断層面上のすべりの立ち上がり時間が短くなったり、破壊伝播速度が速くなると、周期 5 秒以下の速度応答スペクトルは大きくなる。さらに、表層に軟弱な堆積層があると地動は大きく増幅される。東京の下のくぼ地構造により地動の継続時間は大きく増大するが、速度応答スペクトルにはほとんど影響しない。